Pneumatic cells toward absolute Gaussian morphing

Tian Gao, José Bico, Benoît Roman

Pneumatic cells towards absolute Gaussian morphing

Tian Gao,[1] José Bico,[1] Benoît Roman[1*]

[1]Laboratoire de Physique et Mécanique des Milieux Hétérogènes (PMMH),
CNRS, ESPCI Paris, Université PSL, Sorbonne Université, Université Paris Cité,
7 quai St Bernard, Paris, 75005, France
*To whom correspondence should be addressed; E-mail: benoit.roman@espci.fr.

On a flat map of the Earth, continents are inevitably distorted. Reciprocally, curving simultaneously a plate in two directions requires a modification of in-plane distances, as Gauss stated in his seminal theorem. Although emerging architectured materials with programmed in-plane distortions are capable of such shape-morphing, an additional control of local bending is required to precisely set the final shape of the resulting 3D surface. Inspired by bulliform cells in leaves of monocotyledon plants, we show how the internal structure of flat panels can be designed to program simultaneously bending and in-plane distortions when pressurized, leading to a targeted shell shape. These surfaces with controlled stiffness and fast actuation are manufactured using consumer-grade materials, and open a route to large-scale shape-morphing robotics applications.

One-Sentence Summary

Programming simultaneously bending and in-plane distortion of architectured surfaces promotes surface-morphing robotics.

Plants leaves or petals provide remarkable examples of shape morphing induced by differential growth and are a source of inspiration for engineering (*1*). Materials capable of changing shape find numerous applications, ranging from the fabrication of complex micro-structures (*2*), the manipulation of fragile objects (*3, 4*) or soft-robotics devices (*5–8*) to locomotion in complex environments (*9*) or the design of deployable shelters (*10*). While basic grabbing devices rely on bending linear beams through bilayer effects (*11*), shape morphing of surfaces poses a much greater geometrical challenge. If distances along the plane of a surface, ie the metrics, are conserved, its Gaussian curvature (product of its two principal curvatures) is strictly conserved, restricting the achievable shapes to families of isometries (e.g. cylinders or cones for a sheet of paper). General morphing of a surface, such as when a plane takes on a doubly curved shape, referred to here as Gaussian morphing, requires metric distortion (*12*). In natural structures, such metric changes result from differential growth (*13, 14*). Engineered systems rely on equivalent non-homogeneous transformations such as swelling of hydrogels (*15–18*), relaxation of liquid crystal elastomers (*19*) or of prestretched polymeric filaments (*20, 21*), inflatable structures (*22–24*), origami or kirigami tesselation (*25–27*). Although the shape of a surface is rigorously defined by both curvature and metric tensors, these two parameters are generally not addressed simultaneously, except in a few elegant exceptions involving very compliant materials relying on relatively slow swelling actuation (*28–30*). Programming complete morphing in stiff structures with fast actuation that are relevant for engineering applications still remains a challenge.

In the realms of Botany, leaves of monocotyledon plants such as corn are able to curl inward reversibly under dry conditions, limiting evaporation (Fig. 1A). Actuation relies on peculiar bulliform cells that change significantly their volume depending on turgor pressure (*31, 32*),

producing in-plane extension or contraction of one side of the surface leaf. Inspired by this example from Nature, we designed thin panels embedded with inflatable cells referred to as pneumatic Gaussian cells. Both in-plane contraction and angular deflection of the panels can be programmed simultaneously through the cell's design, leading to stiff 3D structures. This qualitative step constitutes an important milestone towards versatile morphing robotics applications.

Contracting and bending simultaneously

The elementary unit of a Gaussian cell is based on trapezoidal channels 3D-printed on a layer of airtight fabric (Fig. 1B). A heat-sealed layer of the same fabric closes the cell (see detailed fabrication process in Supplementary Materials and Movie S1). The different channels embedded in the thin sandwich are connected to a pressure source. Pneumatic actuation of the cells induces the transformation of the initially flat panel into a complex shape such as a curve-folded origami structure (Fig. 1C and Supplementary Movie S1). Figure 2A presents the deployment mechanism of a plate composed of juxtaposed parallel Gaussian cells with spacial periodicity ℓ. As the base and the top of the cells are sealed with highly bendable but inextensible fabric, the cells tend to bulge into circular arcs upon inflation, inducing an inward displacement and rotation of the lateral walls. The general case of symmetric trapezoidal cross-section (in orange) is characterized by the thickness of the plate H, the shortest width W and the internal angle β of the cell walls (see Supplementary Materials for the case of asymmetric cells). The inflated shape of a Gaussian cell is readily obtained from energy minimization (see details in Supplementary Materials). The resulting folding angle γ of the cell is a solution of:

$$\left(\beta - \frac{\gamma}{2}\right) = \sin\beta \cos\left[\left(\beta - \frac{\gamma}{2}\right)\left(\frac{W}{H}\cot\beta + 1\right)\right]. \tag{1}$$

Inflation also reduces the length of the midsegment of the cell by a factor λ (Fig. 2B). This quantity referred to as in-plane contraction is solution of:

$$\lambda = \frac{\cos\left(\beta - \frac{\gamma}{2}\right)}{\left(\beta - \frac{\gamma}{2}\right)\cos\frac{\gamma}{2}} \sin\left[\left(\beta - \frac{\gamma}{2}\right)\left(\frac{W}{H}\cot\beta + 1\right)\right]\left(\frac{W}{H}\cot\beta + 1\right) \tag{2}$$

Two limit cases highlighted in yellow and green in Figure 2 correspond to cells of rectangular ($\beta = 0°$) and triangular ($W/H = 0$) cross-sections that only provide in-plane contraction or deflection, respectively. Experimental values of γ and λ obtained over a wide range of geometrical parameter show an excellent agreement (Fig. 2B and C) with theoretical predictions (Eqs. 1-2). Figure 2C and D presents the wide palette of contraction ratio and folding angle as a function of the geometry of inflatable cells parameterized by their internal angle β and aspect ratio W/H. Large folding angles are found in the upper part of the parameter space, where large internal angles β promote asymmetry across the thickness of the cell, and values as large as $\gamma > 90°$ can be obtained. Largest contraction is intuitively obtained in the lower right corner, for large W/H. Contraction ratio and folding angle are varying along different patterns in the parameter space. For instance, point (ii) in Figs. 2D and E corresponds to the same contraction as point (i) but to a larger folding angle. An important consequence is that arbitrary combinations of (λ, γ) can be programmed.

Stiff pneumatic Gaussian Cell

Gaussian morphing requires large in-plane deformations, and is therefore usually associated with low stiffness (*15, 17, 19, 28*). Pneumatic Gaussian Cells provide remarkable load-bearing capabilities, which can be adjusted by not only pressure but also the geometry of the cell, a feature distinct from traditional inflatable structures. Their stretching stiffness is assessed by testing the mechanical response of a symmetric cell ($\beta = 0°$) loaded in the direction perpendicular to the channels walls (Fig. 3A). Figure 3B shows the tension force F as a function of the

net displacement Δ for a given specimen. The theoretical prediction (see Supplementary Materials) is plotted in continuous lines and match precisely the force-displacement curves measured experimentally. For a given applied pressure P, the effective Young modulus E_c of a single cell is inferred from the linear response of the cell for small displacement, and is expected to follow:

$$E_c = \tan\theta_0 \, \frac{\cos\theta_0 + \theta_0 \sin\theta_0}{\sin\theta_0 - \theta_0 \cos\theta_0} \, P \tag{3}$$

where the initial spanned angle θ_0 obeys $\theta_0/\cos\theta_0 = W/H$ (see Supplementary Materials). The comparison of the normalised modulus E_c/P as a function of the aspect ratio W/H is in excellent agreement with the theoretical prediction, confirming the dependence of the modulus with the applied pressure and the geometry of the cell, solely (Fig. 3C). Conversely, for large extension, the stiffness of the cell (Figure 3B) tends toward the stretching stiffness of the pair of fabric laid flat, $E_{max} = 2E_f\, t/H$ (where E_f and t are the Young modulus and thickness of the fabric sheet), which is independent of pressure.

The angular stiffness of a non-symmetric cell ($\beta \neq 0°$) is obtained by measuring the torque M as a function of the applied deflection angle γ (Figs. 3D and E). The effective angular stiffness K_r of the cell (linearized response) is predicted to obey (see Supplementary Materials):

$$\frac{K_r}{PLH^2} = \frac{W}{H} \frac{\cos(\theta_0 + \beta - \frac{\gamma_0}{2}) + 2\theta_0 \sin(\theta_0 + \beta - \frac{\gamma_0}{2})}{4\theta_0^2 \cos\beta}, \tag{4}$$

where $\theta_0 = \frac{W}{H} \frac{(2\beta - \gamma_0)\cos\beta}{2\sin\beta}$ is the initial value of spanned angle of arc W, L is the length of cell, and the initial folding angle γ_0 follows (Eq. 1).

These predictions (continuous line in Fig. 3F) are confirmed by direct experimental measurements of the angular stiffness (with no adjustable parameter). Different configurations (e.g. points 1 and 2 in the contour map from Fig. 3g are expected to display different actuated geometries but similar structural stiffness (for the same pressure). Overall, we find that the mechanical stiffness of an isolated Gaussian cell is directly proportional to its internal pressure, whereas its

activated geometry is independent of pressure, leaving the possibility to tune the stiffness independently of the shape (see Supplementary Materials for a general discussion of the stiffness of the shell structure as a function of the spatial periodicity of the cells.

Assembling Gaussian Cells into programmable structures

We now explore how elementary folding and contraction mechanisms of individual cells can be used to program shape-morphing of plates into complex structures. The induced curvature can be discretized as $\kappa = \gamma/\ell$, where ℓ is the spacial periodicity of the cells' distribution (Fig. 2A). As a consequence, developable surfaces, such as generalized cylinders or cones, are readily obtained by controlling locally the deflection angle. Figure 4A illustrates different examples where the sign of a constant curvature is alternated by piece, the amplitude of the curvature is proportional to the curvilinear abscissa, or the direction of the bending direction is modified, leading respectively to (i) an "S" shape, (ii) a spiral with linearly increasing curvature or (iii) a curly ribbon (see Movies S2). A developable helicoid is finally obtained by selecting the director lines tangent to a central circle cut inside the initially flat structure, with an additional transverse cut to allow for deployment (Fig. 4B and Movie S2). Fig. 4C and Movie S3 demonstrate with the simple example of a slit annulus morphing into a cone, why curvature and metric changes should be simultaneously used. Programming solely curvature without in-plane contraction on such a slit annulus does lead to a cone (Fig. 4C(i)), but with an overlap angle $\theta^+ = 2\pi(1-\sin\phi)$, where ϕ is the cone angle. Conversely, an annulus with cells solely programmed for in-plane contraction will remain flat when actuated with an angular deficit $\theta^- = 2\pi(1-\lambda_{eff})$, where λ_{eff} is the effective contraction ratio at the scale of the whole structure (Fig. 4C(ii)). Only if both active curvature and in-plane contraction are combined in the programming, do we observe that the annulus deploys into a perfect target conical shape (Fig. 4C (iii)).

In-plane contraction dictates the Gaussian curvature of the deployed structures. However, targeting solely this quantity only restrains the resulting shape to a family of isometries (*12*). In practice, the observed realization relies on a minimization of the finite bending energy of actual structures, which tends to limit the design space to peculiar solutions among these families (*35, 36*). Archetypal catenoid and helicoid - minimal surfaces commonly illustrated with soap films - present the same distribution of Gaussian curvature. Programming solely in-plane contraction using cells of rectangular cross-section is therefore not enough to select between both configurations. However, adjusting the internal angle of the walls allows for the control of the bending curvature in the direction perpendicular to the cells path. As a result two structures designed with similar cell outlines (the zigzag patterns provide bi-axial contraction (*37*)), but precise adjustment of the internal angle lead to the desired helicoid (of programmed handiness) or catenoid shapes respectively (*38*) (Fig. 4D and Movie S4, see Supplementary Materials for the detailed design of the cells). Although Gaussian cells are capable of curvature in the direction perpendicular to their axis, the use of alternating directions overcomes this constraint.

Large efforts have recently been devoted to the design of origami structures (*25, 26*). However, robust self-actuation still remains an issue (*39, 40*). Figure 5A presents a classical Miura-ori tessellation pattern (*41*) where "mountain" and "valley" creases have been programmed using Gaussian cells. Upon inflation, the structure self-folds to the target configuration with a stiffness high enough to support a relatively heavy load (see Movie S5). Beyond origami structures, remarkable stiffness, robustness to failure and fast actuation (see Supplementary Materials for discussion on performances and scalability) bring pneumatic Gaussian cells as a promising principle for applications in morphing robotics. Standard soft-robotics technologies generally rely on bending actuation of grabbing beam elements (*11*). However, robotic systems could be developed harnessing the surface shape morphing achieved with Gaussian cells. Figure 5B illustrates an initially flat disk that adopts in a fraction of second the shape of a crater based on

the cone transformation and traps an object rolling over (see Movie S6 which also demonstrates how a ball can be guided by an active track). Although the presented examples are based on a single inlet and interconnected cells, more complex kinematics could be obtained by separating cells into subgroups that would be activated separately or by embedding mechanical valves between cells that could provide a sequential actuation (*42, 43*). Finally, active surfaces may also be used to manipulate liquids. In Fig. 5C and Movie S7, a long strip is programmed to morph into a curved gutter of positive Gaussian curvature (*37*) with a controlled bending direction, transferring liquid to a different container, and demonstrating the versatile capabilities of the technique.

Towards shape morphing robotics

Inspired by actuating cells observed in some plants, we have developed powerful and versatile Gaussian cells that provide stiff, fast and reversible self-morphing of thin plates. As both metric and curvature can be simultaneously programmed, these cells provide an acurate control of the deployed geometry, imparting a high degree of mechanical stability to the resulting structure. Moreover the stiffness of the deployed shell (proportional to applied pressure) can be tuned independently of its shape (dictated by the local configuration), opening the possibility of developing large scale morphing structures. Pneumatic Gaussian cells combines stiffness to a high level of control in shape-programming, holding significant promise for applications in which avoiding mechanical instabilities is crucial, but also for haptic devices where both shape and stiffness controls are valuable output information for the end user. Made through standard 3D printing techniques with consumer-grade materials, the resulting robust shape-changing surfaces bring the concept of material-machine closer to large-scale and general commodity product.

References

1. H. Liang, L. Mahadevan, *Proc. Natl. Acad. Sci. U. S. A.* **108**, 5516 (2011).

2. X. Cheng, Y. Zhang, *Advanced Materials* **31**, 1901895 (2019).

3. L. Hines, K. Petersen, G. Z. Lum, M. Sitti, *Advanced Materials* **29**, 1603483 (2017).

4. T. J. Jones, E. Jambon-Puillet, J. Marthelot, P.-T. Brun, *Nature* **599**, 229 (2021).

5. R. F. Shepherd, *et al.*, *Proceedings of the national academy of sciences* **108**, 20400 (2011).

6. J. Wang, D. Gao, P. S. Lee, *Advanced Materials* **33**, 2003088 (2021).

7. M. Li, A. Pal, A. Aghakhani, A. Pena-Francesch, M. Sitti, *Nature Reviews Materials* **7**, 235 (2022).

8. Y. Yang, K. Vella, D. P. Holmes, *Science Robotics* **6**, eabd6426 (2021).

9. W. Kim, *et al.*, *Science robotics* **4**, eaay3493 (2019).

10. D. Melancon, B. Gorissen, C. J. García-Mora, C. Hoberman, K. Bertoldi, *Nature* **592**, 545 (2021).

11. B. Gorissen, *et al.*, *Advanced Materials* **29**, 1604977 (2017).

12. D. J. Struik., *Lectures on Classical Differential Geometry* (Cambridge, Mass.: Addison–Wesley Press, Inc, 1950).

13. J. Dervaux, M. B. Amar, *Physical review letters* **101**, 068101 (2008).

14. A. B. Rebocho, P. Southam, J. R. Kennaway, J. A. Bangham, E. Coen, *Elife* **6** (2017).

15. Y. Klein, E. Efrati, E. Sharon, *Science* **315**, 1116 (2007).

16. E. Efrati, E. Sharon, R. Kupferman, *Phys. Rev. E* **80**, 016602 (2009).

17. J. Kim, J. A. Hanna, M. Byun, C. D. Santangelo, R. C. Hayward, *science* **335**, 1201 (2012).

18. A. Nojoomi, J. Jeon, K. Yum, *Nature communications* **12**, 1 (2021).

19. H. Aharoni, Y. Xia, X. Zhang, R. D. Kamien, S. Yang, *Proceedings of the National Academy of Sciences* **115**, 7206 (2018).

20. T. van Manen, S. Janbaz, A. A. Zadpoor, *Mater. Horiz.* **4**, 1064 (2017).

21. J. Gu, *et al.*, *Proceedings of the 2019 CHI Conference on Human Factors in Computing Systems* (2019), pp. 1–10.

22. J. Pikul, *et al.*, *Science* **358**, 210 (2017).

23. E. Siéfert, E. Reyssat, J. Bico, B. Roman, *Nat. Mater.* **18**, 24 (2019).

24. E. Siéfert, E. Reyssat, J. Bico, B. Roman, *Soft Matter* **16**, 7898 (2020).

25. L. H. Dudte, E. Vouga, T. Tachi, L. Mahadevan, *Nature materials* **15**, 583 (2016).

26. S. J. Callens, A. A. Zadpoor, *Materials Today* **21**, 241 (2018).

27. G. Choi, L. H. Dudte, L. Mahadevan, *Nature materials* **18**, 999 (2019).

28. A. Sydney Gladman, E. A. Matsumoto, R. G. Nuzzo, L. Mahadevan, J. A. Lewis, *Nature materials* **15**, 413 (2016).

29. J. W. Boley, *et al.*, *Proceedings of the National Academy of Sciences* **116**, 20856 (2019).

30. S.-J. Jeon, R. C. Hayward, *Soft Matter* **16**, 688 (2020).

31. S. Matschi, *et al.*, *Plant direct* **4**, e00282 (2020).

32. A. Mader, M. Langer, J. Knippers, O. Speck, *Journal of the Royal Society Interface* **17**, 20200358 (2020).

33. S. D. Guest, S. Pellegrino, *Proceedings of the first international seminar on structural morphology* (1992), vol. 25.

34. D. Webb, *et al.*, *Starshade Mechanical Architecture & Technology Effort*.

35. E. Efrati, E. Sharon, R. Kupferman, *Journal of the Mechanics and Physics of Solids* **57**, 762 (2009).

36. S. Armon, E. Efrati, R. Kupferman, E. Sharon, *Science* **333**, 1726 (2011).

37. T. Gao, E. Siéfert, A. DeSimone, B. Roman, *Advanced Materials* **32**, 2004515 (2020).

38. H. Aharoni, E. Sharon, R. Kupferman, *Physical review letters* **113**, 257801 (2014).

39. C. D. Santangelo, *Annual Review of Condensed Matter Physics* **8**, 165 (2017).

40. S. Wu, T. Chen, H. Tsai, *Journal of Mechanics* **35**, 627 (2019).

41. M. Schenk, S. D. Guest, *Proceedings of the National Academy of Sciences* **110**, 3276 (2013).

42. L. Jin, A. E. Forte, K. Bertoldi, *Advanced Science* **8**, 2101941 (2021).

43. L. C. van Laake, J. de Vries, S. M. Kani, J. T. Overvelde, *Matter* **5**, 2898 (2022).

Acknowledgments

We thank Hillel Aharoni and Antonio DeSimone for stimulating discussions and Bruno Moulia for botanical inspiration.

Funding: This work was partly supported by French ANR SecondSkin project (ANR-21-CE33-0018) .

Author contributions: T.G., J.B., and B.R. conceived and developed the Pneumatic Gaussian Cell concept. T.G., J.B., and B.R. conducted the experiments and analysed the data. T.G., J.B., and B.R. developed the theoretical model. All authors wrote the manuscript.

Competing interests: The authors declare no competing interests.

Data and materials availability: All data are available in the main text or Supplementary Materials.

Supplementary Materials

Materials and Methods

Supplementary Text

Figs. S1 to S20

Movies S1 to S7

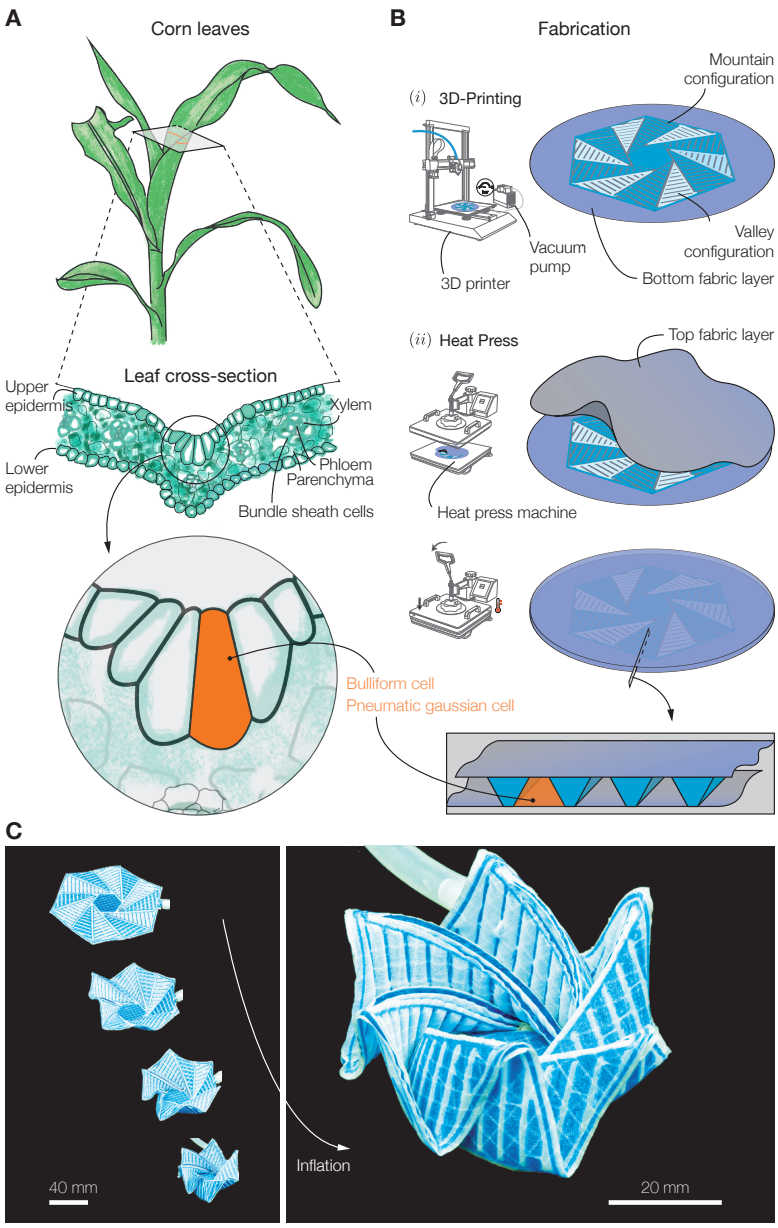

Figure 1: **From leaf Bulliform cell to Pneumatic Gaussian Cell. (A)** Leaves of corn open or close as a function of weather conditions by inflating of deflating bulliform cells under turgor pressure. **(B)** Fabrication of shape morphing structure based on Pneumatic Gaussian cells. (i) Tilted Thermoplastic Polyurethane (TPU) walls are 3D-printed over a first layer of TPU coated fabric. (ii) Gaussian cells (orange) are formed by sealing a second layer of fabric on the top of the structure with a heating press. **(C)** Upon inflation (see Movie S1), an initially flat panel composed of programmed Gaussian cells self-shapes into a complex 3D structure inspired by Starshade project (*33, 34*).

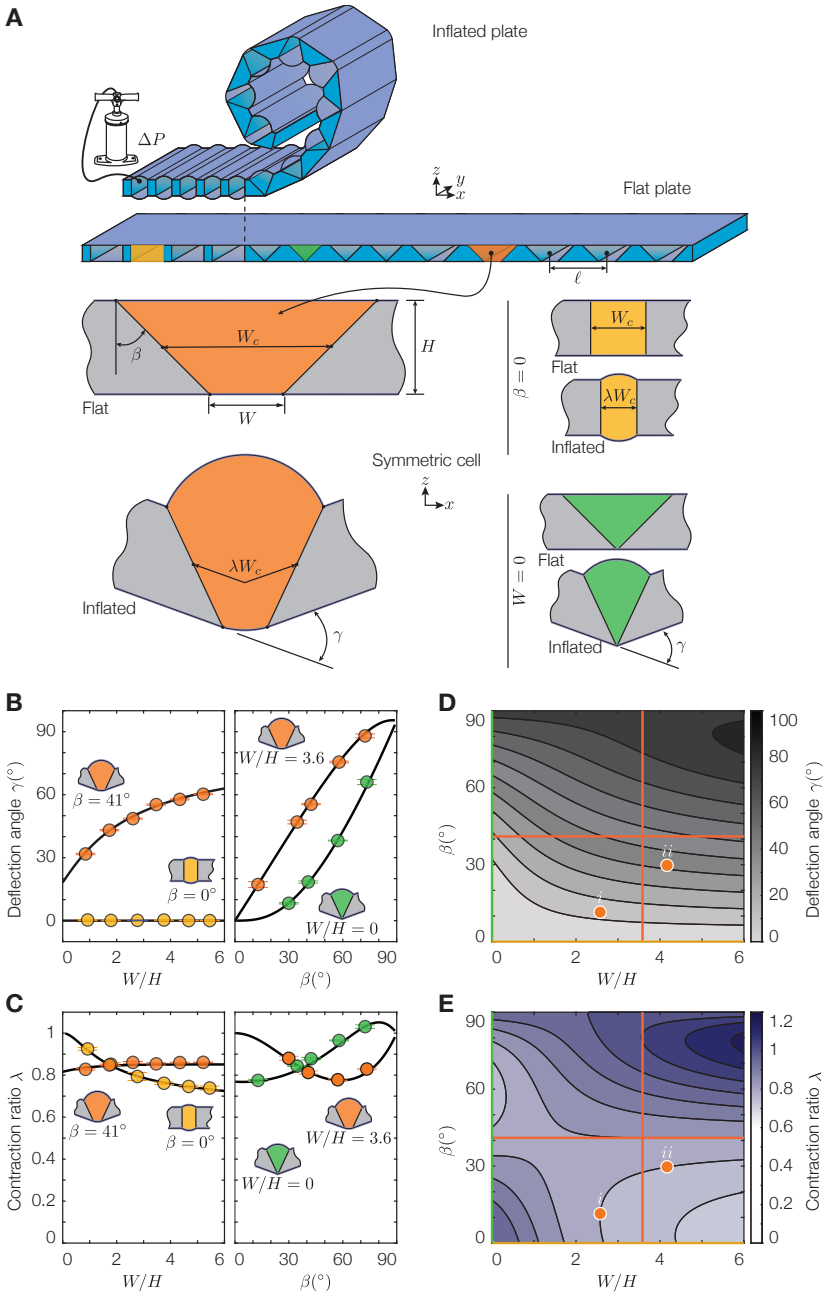

Figure 2: **Programming deformation of Gaussian cells. (A)** Schematic illustration of the the deployment of a flat plate based on three types of symmetric cells. Generic trapezoidal cell (orange) with walls of thickness H tilted by an angle β and separated by a distance W. Upon inflation, the cell induces a local deflection γ and a contraction λ with respect to the median line W_c. Rectangular cell (yellow) and triangular cell (green) configurations correspond to vertical walls ($\beta = 0$) or to contacting bases ($W = 0$), respectively. **(B,C)** Deflection angle γ and contraction ratio λ as a function of the dimensionless width W/H and of the tilt angle β, for fixed values of β or W/H, respectively. Solid black lines correspond to theoretical predictions (Eqs. 1 & 2). **(D,E)** Landscape of programmable deformations. Theoretical contour maps of the contraction ratio λ and deployed angle γ in a general configuration.

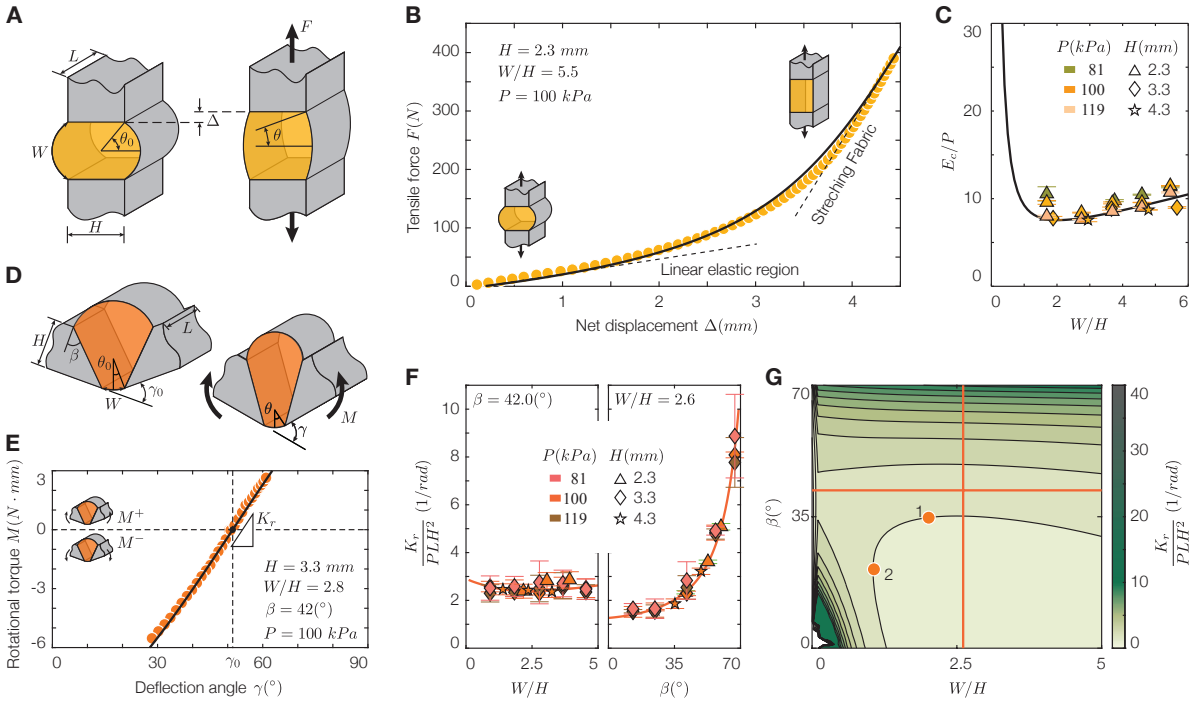

Figure 3: **Mechanical properties of an inflated cell. I. Stretching modulus**: **(A)** Inflated rectangular cell at rest and under tension with span angle θ and net displacement Δ. **(B)** Force-displacement curve of an inflated rectangular cell of height $H = 2.3\,\text{mm}$, dimensionless width $W/H = 5.5$ under a pressure $P = 10.0\,\text{kPa}$ (solid yellow circles). Comparison with theoretical prediction (solid black line). **(C)** Dimensionless stretching modulus E_c/P as a function of dimensionless width W/H for various pressures and different cell height. Comparison with theoretical prediction from Eq. 3 (solid black line). **II. Bending stiffness**: **(D)** Bending test of of an inflated trapezoidal cell. **(E)** Starting from an equilibrium deflection angle γ_0, applying a torque M results in a new angle γ ($H = 3.3\,\text{mm}$, $W/H = 2.78$, $\beta = 41.5°$, $P = 10.0\,\text{kPa}$). The slope of the curve in the vicinity of $\gamma_0 = 50.8°$ corresponds to the rotational stiffness K_r. **(F)** Rescaled rotational stiffness, K_r/PLH^2 as a function of the dimensionless width W/H ($\beta = 42.0°$) and of the angle β ($W/H = 2.6$) at various pressures and different cell heights, respectively. Solid orange lines show our nonlinear theoretical prediction (Eq. 4). **(G)** Contour map of the dimensionless rotational stiffness as a function of W/H and β.

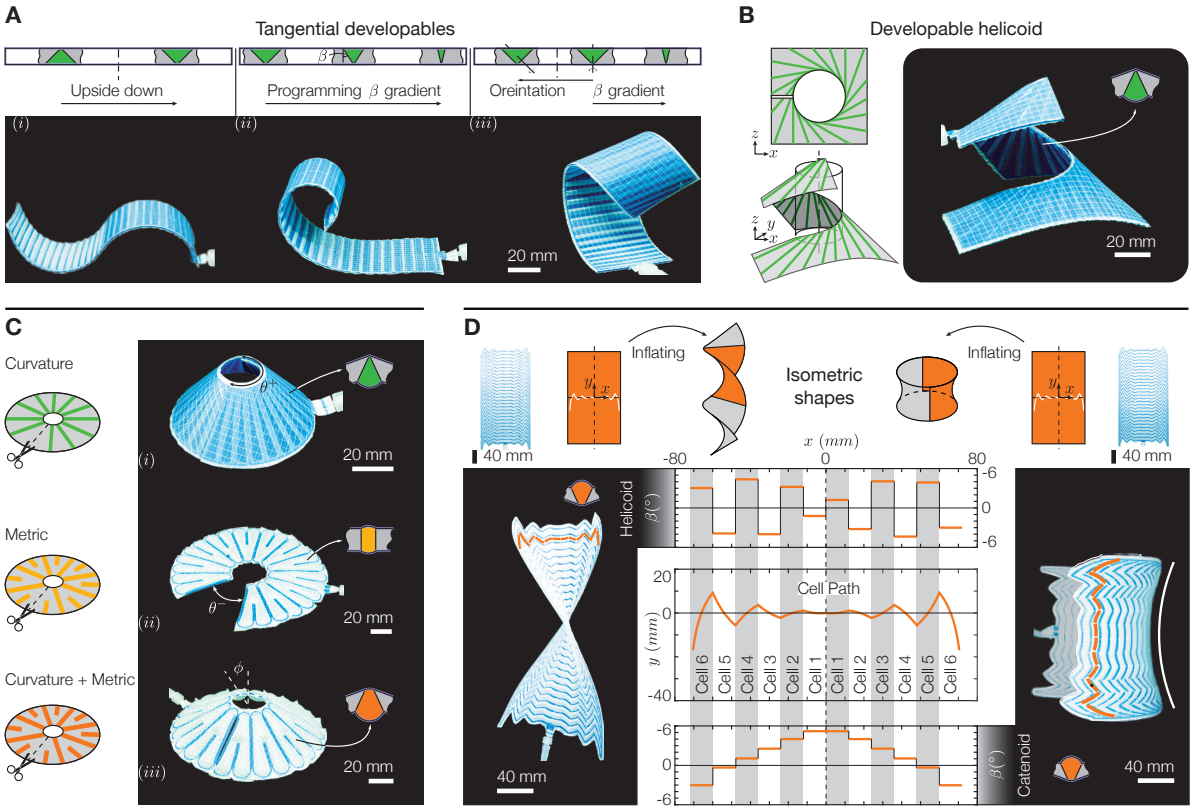

Figure 4: **Programming bending and Gaussian curvatures in multicellular structures (A)** Developable shapes based on triangular-cells (see Movie S2). (i) "S" shape with opposite curvatures; (ii) Spiral with a linearly increasing curvature; (iii): Curling shape with variable curvature direction; **(B)** Developable helicoid with generating lines tangent to the central circle (see Movie S2). **(C)** A sectioned annulus with a radial cells can morph into (i) a truncated cone with angular surplus (pure bending with triangular cells) ; (ii) a flat annulus sector with angular deficit (metric change with rectangular cells); (iii) a perfect truncated cone when bending and metric changes programmed simultaneously (see Movie S3). **(D)** Selection between isometries (see Movie S4). The same metric change (programmed zigzag pattern) leads to degenerated isometric shapes from helicoid to catenoid. Controlling local bending breaks the degeneracy (see inverse programming in Supplementary Material).

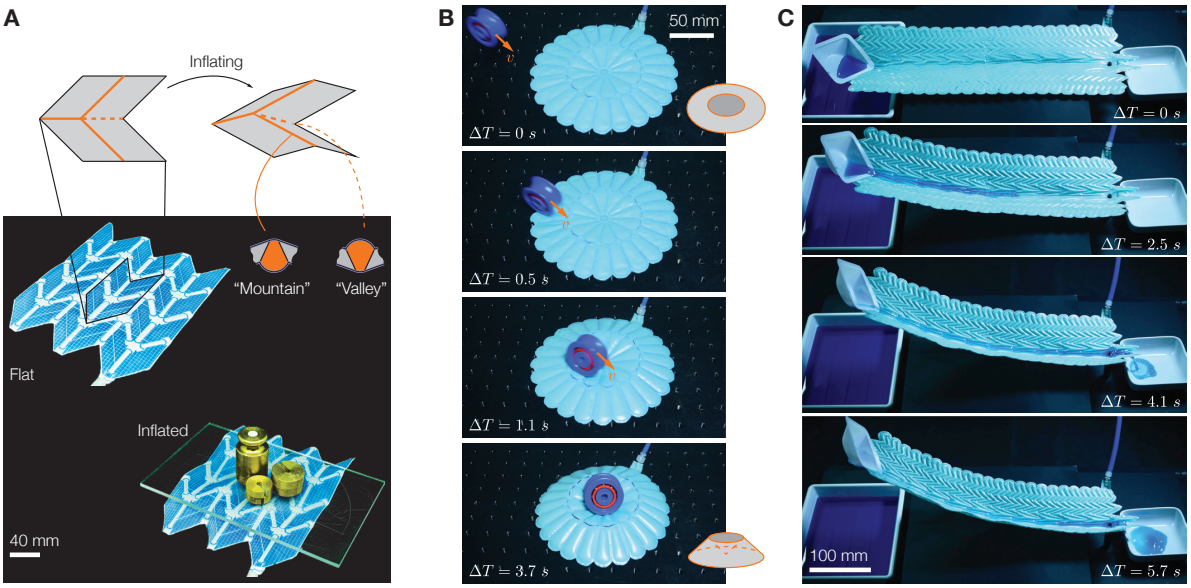

Figure 5: **Towards shape morphing robotics (A)** Self-actuated Miura-ori panel (see Movie S5). Cells function as stiff "mountain" or "valley" creases (total load of 1 kg). **(B)** Volcano shaped actuator (see Movie S6). The initially flat disk is actuated in a fraction of second as a cylinder rolls over it at 10 cm/s. The cylinder (weight 40 g) remains trapped inside the deployed crater. **(C)** Upon inflation, a flat stripe bends into a doubly-curved gutter track that permits manipulation and transport of liquids (see Movie S7).

Supplementary Materials for

Pneumatic cells towards absolute Gaussian morphing

Tian Gao, José Bico, Benoît Roman*

*Corresponding author: benoit.roman@espci.fr.

The PDF file includes:

Materials and Methods

Supplementary Text

Figs. S1 to S20

Supplementary Materials for this manuscript include the following:

Movies S1 to S7

Contents

1 Materials and Methods

In this section, we provide details of the fabrication process of Gaussian cells illustrated in Fig. S1 and Movie 1. A Nylon fabric coated with a layer of thermoplastic TPU (Honeycomb pattern 70 den, thickness of 0.15 mm, weight per unit surface of $150\,\mathrm{g/m^2}$ and Young modulus of 140 MPa) is first placed on the platform of a 3D printer. The piece of fabric is maintained flat on the printing bed by suction, which prevents it from sliding on the platform or from forming wrinkles.

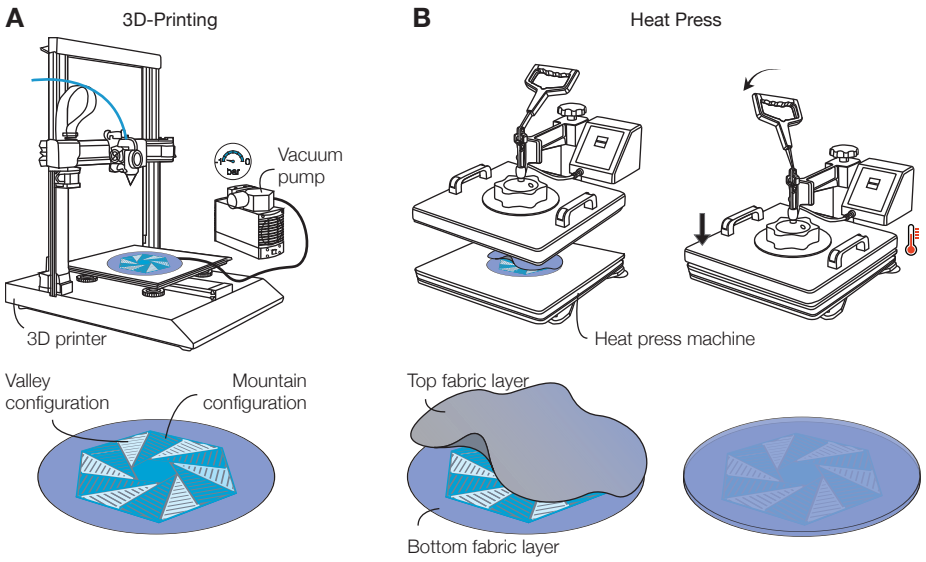

Figure S1: Fabrication methodology of Pneumatic Gaussian Cells. (A) A network of Thermoplastic Polyurethane (TPU) cells with tilted walls are 3D-printed on a layer of TPU coated fabric. During the printing process, the fabric is maintained in place by suction. Small apertures through the walls connect the different cells. **(B)** A second layer of fabric is sealed on the top of the structure with a heat press. See Movie S1 for a description of the fabrication technique.

We print TPU walls on the first layer of the fabric with a fused filament 3D printer (Artillery Sidewinder X2, nozzle diameter of 0.4 mm). For the filament, we used Kimya TPU-92A of diameter 1.75 mm, tensile modulus of 90 MPa. The 3D-printed TPU walls are designed using OpenScad software and sliced with Ultimaker Cura software. To obtain optimal bonding be-

tween the 3D-printed TPU building blocks and the TPU coating layer of fabric sheet, we tune the printing parameters based on tests (bed temperature $76°$C, nozzle temperature $210°$C and printing speed 12 mm/s). When printing is finished, the structure is removed from the printing bed and fixed on a 3 mm thick rigid glass plate with double-sided tape. Next, we close the printed structure by the second flat fabric sheet, with boundaries are taped on the glass plate. This second fabric sheet is finally bonded on the top of the printed structure with a heat press (heating temperature of $184°$C for 10 s). As a result, airways are formed between the two fabric membranes, surrounded by TPU building blocks. Upon inflation, air pressure tends to maximize the volume of each individual cell and the whole structure may morph into a complex 3D shape.

The robustness of our structures is typically the same as in most inflatable equipment based on airtight fabrics. In contrast with a rubber balloon, the membrane is almost inextensible. As a consequence, a local puncture in one cell generally does not lead to a catastrophic rupture (indeed propagating a crack does not release much elastic energy and the "ripstop" nylon fabric selected for our cells is particularly tough). Membranes of low extensibility are particularly easy to mend by applying a flexible patch with sufficiently good adhesion.

In the multi-cell structures discussed here, all the cells were interconnected by internal channels embedded in the 3D printed TPU plates. A loss of pressure in one cell would then deflate all the cells. For a better robustness it is however possible to compartmentalize the cells into independent sections, as is customary with inflatable boats for instance. Another possibility is to implement the internal communication channels with one-way valves that maintain internal pressure of cells even if the neighboring cell looses pressure.

2 Geometry of a pneumatic Gaussian cell

Laser triangulation method

The geometrical characterisation of a Pneumatic Gaussian Cell upon actuation was inferred from monitoring the intersection of a laser sheet with the structure. The principle is very simple: a cylindrical lens placed in front of a laser beam produces a sheet of light projected with an oblique incidence to the structure. The profile of the intersection of the laser sheet with the surface is geometrically related to the local topography. Viewed from above, the distortions of this line are directly proportional to the height profile of the surface through a simple trigonometric relation (Fig. S2):

$$H = h \tan \phi \tag{1}$$

where h is the observed shift of the laser line. Images are captured with a digital camera (Nikon D850) and analysed with ImageJ software. Using this method, we first measure precisely the geometrical parameters of a single printed cell before bonding the top fabric sheet (printed height H, shortest width W, internal angle β). Next, we measure geometrical parameters of an inflated cell (folding angle γ, contraction ratio λ).

Geometry of symmetric cell

Theoretical model based on force balance approach: We aim at modelling the geometrical deployment induced by the pressurization of a general symmetric Pneumatic Gaussian Cell. We respectively define H as the cell height, W as the length of short edge AB, W' as the length of long edge CD, W_c as the length of midsegment EF, and β as the slope of the cell wall with respect to the vertical direction (Fig. S3A).

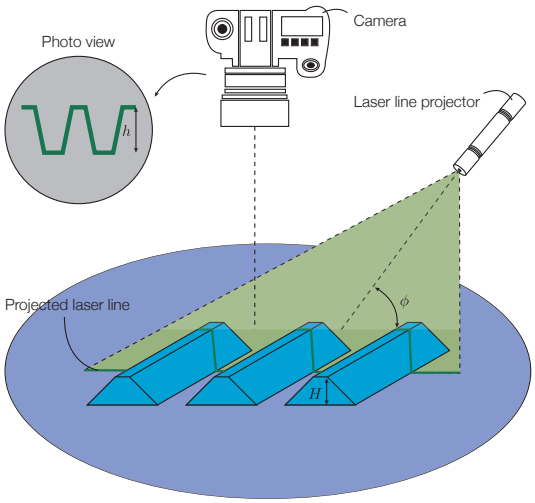

Figure S2: Schematic of setup for laser triangulation method.

Similarly, the length of midsegment is given by:

$$W_c = W + H \tan \beta \tag{2}$$

The flat configuration can thus be totally described by the triplet of variables (H, W, β).

We assume the fabric membrane to be inextensible, but infinitely bendable. We thus expect the cell to maximize its volume upon inflation, forming a droplet-like arc shape and leading to a rotation of the cell walls. We are interested in the resulting inflated shape, that is, the folding angle γ and in-plane contraction factor λ corresponding to the change in length of the midsegment (Fig. S3B). Under this assumption, the lengths of the short arc AB and of the long arc CD remain W and W', respectively. In this symmetric configuration, the shape remains symmetrical with respect to the $O - O'$ axis. Following basic geometry, we obtain:

$$W_0 \sin \alpha = R_2 \sin \theta_2 - R_1 \sin \theta_1 \tag{3}$$

where $W_0 = H/\cos \beta$ is the length of the walls, θ_1 is the half span angle and $R_1 = W/2\theta_1$ is the corresponding radius of short arc AB, θ_2 is the half span angle and $R_2 = W'/2\theta_2$ is the corresponding radius of long arc CD. Finally, α corresponds to the internal angle between BC

and the vertical direction.

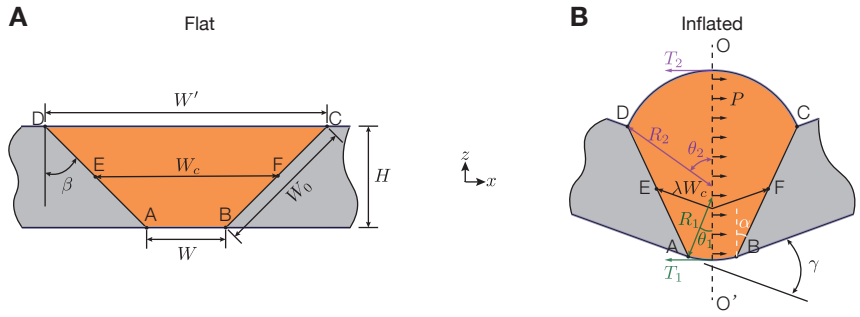

Figure S3: Schematic cross-section of a symmetric cell before and after inflation.

A simple geometrical relation relates the lengths to the thickness of the cell:

$$W' = W + 2H\tan\beta \tag{4}$$

In a cross-section along the axis of symmetry $O - O'$, we balance the force resulting from the pressure P with the tensile force acting on the both fabric arcs, T_1 and T_2:

$$T_1 + T_2 = P[R_1(1-\cos\theta_1) + W_0\cos\alpha + R_2(1-\cos\theta_2)] \tag{5}$$

In addition, the torque balance between the torque resulting from the tensile forces T_1, T_2 and the pressure P with respect to the central point of $O - O'$, results into:

$$(T_2 - T_1)[R_1(1-\cos\theta_1) + W_0\cos\alpha + R_2(1-\cos\theta_2)] = 0 \tag{6}$$

The induced curvature and tension in the membrane are related to the applied pressure through the equivalent of Laplace law for surface tension:

$$P = \frac{T_1}{R_1} = \frac{T_2}{R_2} \tag{7}$$

Combining Eq. 3 and Eqs. 5-7, we can express α as a function of the variables (H, W, β).

$$\alpha = \sin\beta\cos\left[\alpha\left(\frac{W}{H\tan\beta} + 1\right)\right] \tag{8}$$

From basic geometry, we obtain:

$$\gamma = 2(\beta - \alpha) \tag{9}$$

After inputting Eq. 9 into Eq. 8, we can express the folding angle γ as a function of the variables (H, W, β).

$$\left(\beta - \frac{\gamma}{2}\right) = \sin\beta \cos\left[\left(\beta - \frac{\gamma}{2}\right)\left(\frac{W}{H}\cot\beta + 1\right)\right] \tag{10}$$

We now focus on the midsegment. The contraction ratio λ can be expressed as:

$$\lambda = \frac{|EG| + |FG|}{W_c} \tag{11}$$

where $|EG|$ and $|FG|$ are the length of segments EG and FG in the inflated configuration, which are given by:

$$|EG| = (W' - W)\,\frac{\sin\theta_1}{4\,\alpha\cos\frac{\gamma}{2}} \qquad |FG| = (W' - W)\,\frac{\sin\theta_2}{4\,\alpha\cos\frac{\gamma}{2}} \tag{12}$$

with

$$\theta_1 = 2\alpha\,\frac{W}{W' - W} \quad \text{and} \quad \theta_2 = 2\alpha\,\frac{W'}{W' - W} \tag{13}$$

Combining Eq. 11 and Eq. 12, one can express λ as:

$$\lambda = \frac{\cos\left(\beta - \frac{\gamma}{2}\right)}{\left(\beta - \frac{\gamma}{2}\right)\cos\frac{\gamma}{2}} \sin\left[\left(\beta - \frac{\gamma}{2}\right)\left(\frac{W}{H}\cot\beta + 1\right)\right]\left(\frac{W}{H}\cot\beta + 1\right) \tag{14}$$

Theoretical model based on volume maximization: An alternate way to predict the shape of the inflated cell consists in maximizing the volume of the cell for a given applied pressure. We still restrain ourselves to the "inextensible" regime, for which the total potential energy reads:

$$U = -PV \tag{15}$$

where V is the equilibrium volume that corresponds to the shape which minimizes the energy. Equivalently, it maximizes the volume V of the cell shape in inflated configuration. The volume

(per unit width) reads:

$$V = W^2 \frac{\theta_1 - \sin\theta_1 \cos\theta_1}{4\theta_1^2} + W'^2 \frac{\theta_2 - \sin\theta_2 \cos\theta_2}{4\theta_2^2} + \frac{\cos\alpha}{\cos\beta}\left(WH\frac{\sin\theta_1}{2\theta_1} + W'H\frac{\sin\theta_2}{2\theta_2}\right) \tag{16}$$

The maximization problem (including Eq. 13) is finally solved by using Matlab nonlinear optimization toolbox with the constraints $\theta_1 + \alpha \leq \pi/2$ and $\theta_2 - \alpha \leq \pi/2$.

Geometry of asymmetric cells

Theoretical model based on force balance approach: Although the different examples from the main text illustrate symmetric cell, non-symmetric configurations are also possible. We here examine the case of antisymmetric Pneumatic Gaussian Cell, where H is the cell height, W is the width of edge AB and CD, β as the internal angle between vertical direction and AD. When such asymmetric cells are activated, a shear deformation is induced, with the contraction $\lambda_{\parallel}$ in horizontal direction and the contraction $\lambda_{\perp}$ in vertical direction. Remarkably, folding deformation disappears in this case (Fig. S4).

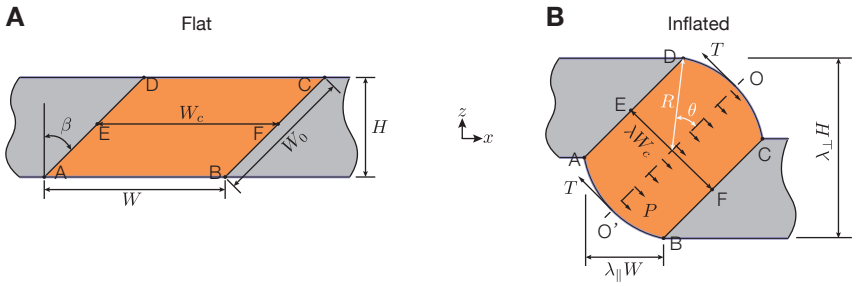

Figure S4: Schematic cross-section of an antisymmetric cell before and after inflation.

We start by focusing on the direction of the symmetry axis $O - O'$. Similarly to the symmetric case (Eq. 5), the balance of the force resulting from the pressure P with the tensile forces in the

fabric membranes (AB and CD) results into:

$$2T = P[2R(1 - \cos\theta) + W_0] \tag{17}$$

where T is the tensile force in the fabric membrane (AB and CD). θ is the half span angle and $R = W/\theta$ is the corresponding radius of arc AB and CD. W_0 is the length of AD and BC. Inputting $W_0 = H/cos\beta$ into Eq. 7, we obtain:

$$\frac{\theta}{\cos\theta} = 2\,\frac{W}{H}\cos\beta \tag{18}$$

The span angle θ can finally be obtained as a function of the set of variables (H, W, β).

Once θ has been determined, the contraction ratio of the mid-segment EF can be inferred from simple geometry:

$$\lambda = \frac{\sin\theta}{\theta} \tag{19}$$

The projection of this contraction ratio in horizontal and vertical directions respectively read:

$$\lambda_{\parallel} = \lambda\cos\beta \;\text{ and }\; \lambda_{\perp} = 1 + \frac{W}{H}\lambda\sin\beta \tag{20}$$

3 Mechanics of a pneumatic Gaussian cell

In addition to the shape transformations, controlling mechanical strength is critical to guarantee structural integrity and scaling up or down our system to a wide range of potential applications. In this section, we describe the stiffness of an individual symmetric cell through tensile and flexion tests.

Mechanical testing

To quantify the evolution of mechanical properties as a function of cell geometry, tensile and flexion tests were performed with a force-displacement test machine (Instron 5865). In tensile

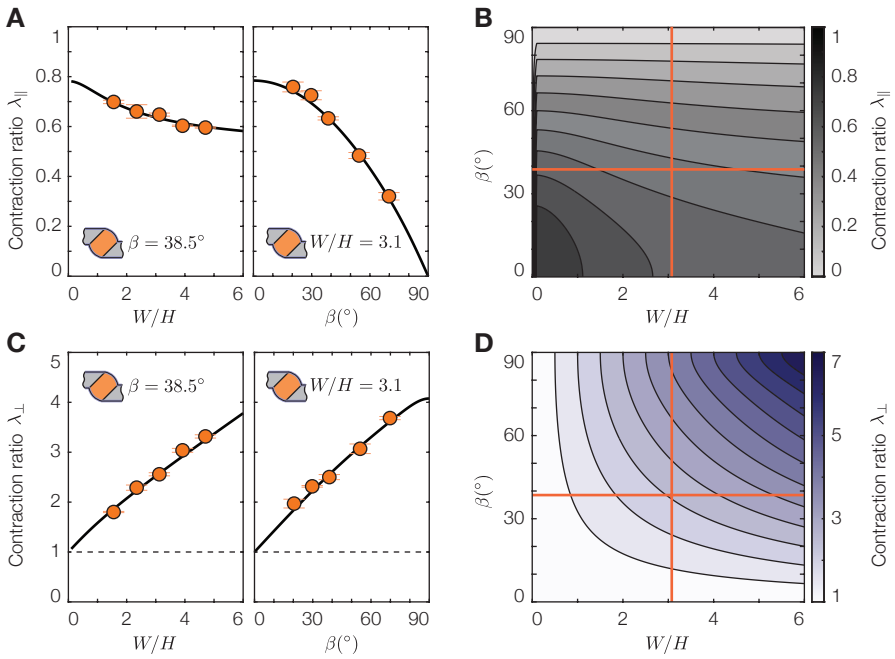

Figure S 5: **(A)** Contraction ratio $\lambda_{\parallel}$ measured experimentally (with theoretical predictions in solid lines) as a function of the non-dimensional length W/H or tilt angle, β, for fixed values of β or W/H, respectively. **(B)** Landscape of variations of $\lambda_{\parallel}$ as a function of W/H and β. **(C)** Contraction ratio $\lambda_{\perp}$ measured experimentally (with theoretical predictions in solid lines) as a function of the non-dimensional length W/H or tilt angle, β, for fixed values of β or W/H, respectively. **(D)** Evolution of the contraction ratio $\lambda_{\perp}$ as a as a function of W/H and β.

tests (on symmetric cells with different W and $\beta = 0°$), the cells are clamped along their TPU walls to the load cell and the to the base of the machine. For flexion tests, L-shape structures were 3D-printed in PLA to apply positive and negative torque.

Stretching stiffness of the symmetric cell ($\beta = 0°$)

Theoretical model: Consider a rectangular cell of length L (in the direction perpendicular to the plane of view, Fig. S7A), width W, height H, internal angle $\beta = 0$, and thickness of fabric t, with $t \ll W \ll L$. Upon inflation, if $P \geq Et^3/W^3$, that is, if the pressure energy is large compared to the bending energy of the fabric sheet - which is the case in our experiments - the

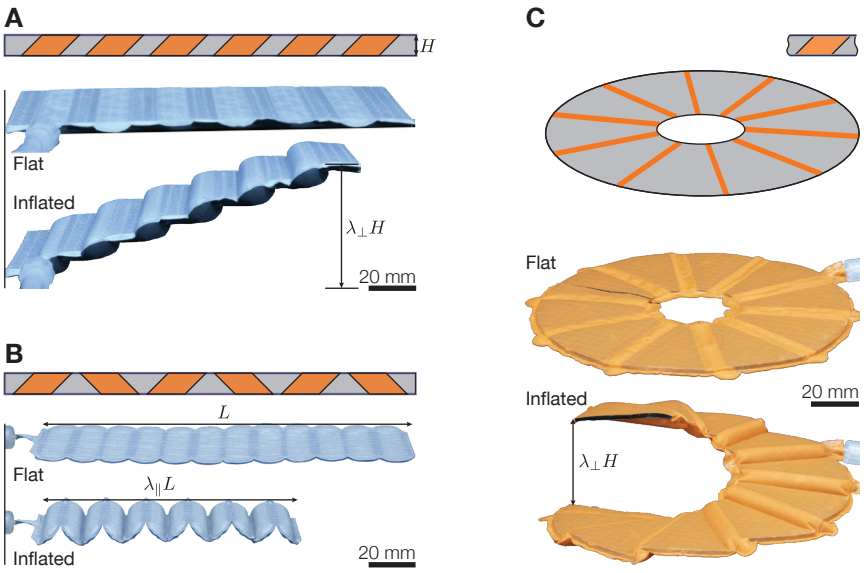

Figure S 6: Examples of structures using anti-symmetric cells: (A, C) Self-deploying stair cases or **(B)** High contraction beam ($\lambda_\parallel = 0.7$) obtained with alternate cells.

cell tends to maximize its volume. Both fabric membranes bend to form a droplet-like arc shape with radius R_0 and half span angle θ_0.

Following basic geometry, we obtain:

$$W = 2R_0\theta_0 \tag{21}$$

We now consider the edge of the cell walls AD. Balancing the force induced from the pressure P with the tensile force in the fabric membrane (AB and CD) results into:

$$PH = 2T_0 \cos\theta_0 \tag{22}$$

The tension in the fabric is related to the pressure and the radius of curvature of the inflated bulge through Laplace law:

$$T_0 = PR_0 \tag{23}$$

Although we considered the fabric as inextensible in the previous chapter, we can account here

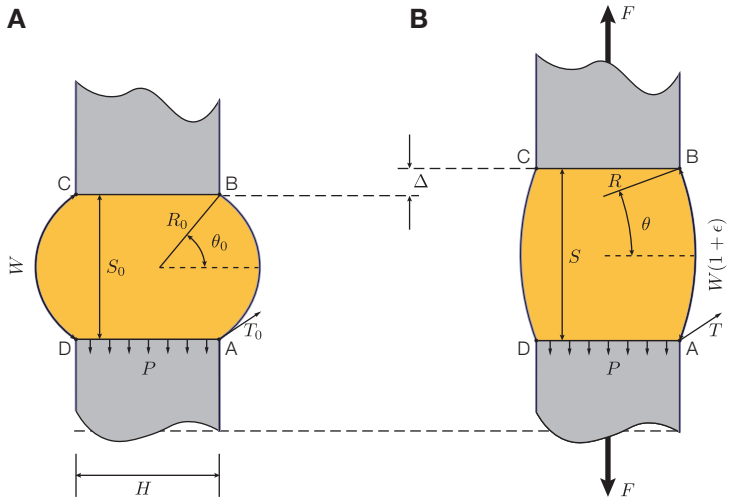

Figure S 7: Stretching of asymmetric cell ($\beta = 0$) in a direction perpendicular to the walls: (A) Cross-section of an inflated cell at rest and **(B)** under traction. Applying a stretching force F leads to a displacement Δ and to an opening of the span angle θ. In addition to the global change of the cell shape, we may consider a finite extensibility of the fabric, leading to a strain ϵ when under tension.

for a finite strain ϵ upon a stretching force F.

Laplace's law imposes the cross-sections of the cell of initial half span angle θ_0 to remain portions of circles of half span angle θ and corresponding radius of curvature $R = W(1+\epsilon)/\theta$, where ϵ is the (uniform) strain induced to the fabric sheet by the tension T (Fig. S7B):

$$T = PR = \frac{PW(1+\epsilon)}{2\theta} \tag{24}$$

In addition, the induced strain in the fabric is related the tension T:

$$T = Et\epsilon \tag{25}$$

where t is the thickness of fabric.

A simple force balance provides the following expression for the force F (per unit length):

$$F + PH = 2T\cos\theta \tag{26}$$

The corresponding total displacement Δ reads:

$$\Delta = S - S_0 = W\left((1+\epsilon)\frac{\sin\theta}{\theta} - \frac{\sin\theta_0}{\theta_0}\right) \tag{27}$$

Combining Eqs. 21-26, finally leads to an expression for the pulling force F (per unit length) as a function of θ:

$$F = \frac{2PW\cos\theta}{2\theta - \Sigma} - PH \tag{28}$$

where $\Sigma = \frac{PW}{Et}$ is a small dimensionless number as discussed above.

The initial span angle θ_0 can be derived from $W/Hcos\theta_0 = \theta_0$ following Eqs. 21-23. The relation between the total displacement Δ and θ is finally inferred from the combination of Eqs. 24, 25 and Eq. 27:

$$\Delta = W\left(\frac{2\sin\theta}{2\theta - \Sigma} - \frac{\sin\theta_0}{\theta_0}\right) \tag{29}$$

Linearizing the ratio $\frac{FW\sin\theta_0}{\Delta LH\theta_0}$ (where L is the cell length) around the unloaded inflated state (θ_0), we extract an analytical expression for the effective stretching modulus perpendicular to the cell direction for a small infinitesimal deformation:

$$E_c = \tan\theta_0 \frac{\cos\theta_0 + \theta_0\sin\theta_0}{\sin\theta_0 - \theta_0\cos\theta_0} P \tag{30}$$

For minor deformations (as illustrated by the linear elastic region in Fig. 3B), it is reasonable to treat the fabric as inextensible. Consequently, the stretching modulus E_c is independent of the material and is solely determined by the pressure and geometry of the cell. Nonetheless, under significant deformations ($\theta \to 0$), the radius of curvature R expands, causing an increase in fabric tension $T = PR = PW/2\theta$. Eventually, the assumption of inextensibility for the fabric sheet no longer holds and the maximum slope thus corresponds to the stretching modulus of the fabric as shown in Fig. 3B ("stretching fabric"):

$$E_{max} = 2\frac{E_f\, t}{H} \tag{31}$$

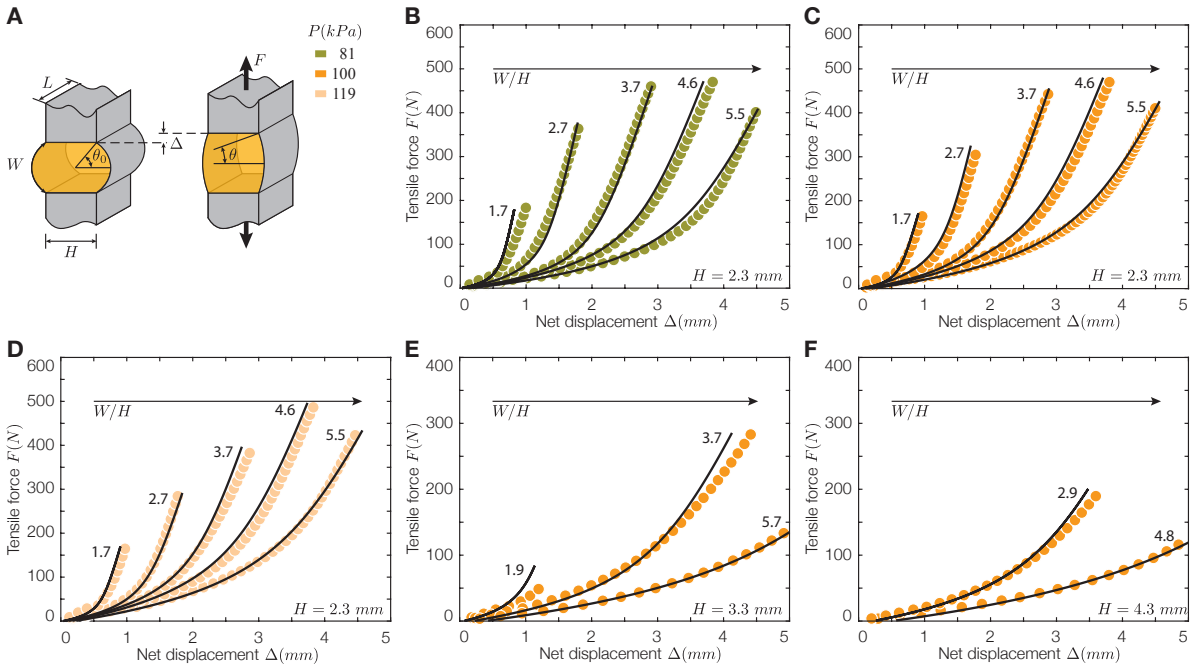

Figure S 8: Stretching an inflated cell. **(A)** Inflated rectangular cell at rest and under tension with span angle θ and net displacement Δ. **(B-F)** Force-displacement curve of an inflated rectangular cells of different heights H and dimensionless widths W/H and for different pressures P (green data, 81 kPa; orange, 100 kPa; pink, 119 kPa). Comparison with theoretical prediction (solid black lines).

where E_f is the young modulus of the fabric. Experimental measurements are in good agreement with this simple argument (Fig. 3B and Fig. S8).

Bending stiffness of the symmetric cell

How does the structure resist to an applied torque? We consider an inflated symmetric cell ($\beta \neq 0°$) where a torque M is applied in the direction perpendicular to the walls. By convention, a negative torque tends to open the cell (γ decreases) while a positive torque tends to close the cell is caused by negative torque and closing the cell (γ increase) as sketched in Fig. S9.

Theoretical model: We consider an inflated symmetric cell ($\beta \neq 0°$) of length L, height H, internal angle β, the length of short edge $AB = W$, the length of long edge $CD = W'$, and the

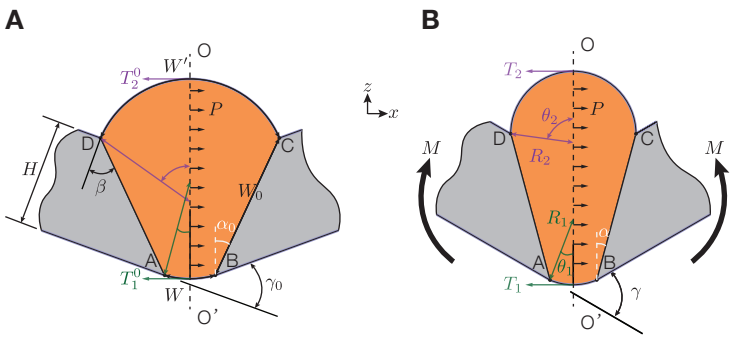

Figure S9: Schematic cross section of an inflated cell submitted to a torque M.

length of the edges AD and $BC = W_0$.

From elementary geometry, we obtain:

$$W_0 \sin\alpha = R_2 \sin\theta_2 - R_1 \sin\theta_1 \tag{32}$$

$$W = 2R_1\theta_1 \tag{33}$$

$$W' = 2R_2\theta_2 \tag{34}$$

$$W_0 = \frac{H}{\cos\beta} \tag{35}$$

where R_1 and R_2 are the inner radii of arc AB and CD and θ_1 and θ_2 the corresponding half spanned angles. α corresponds to the internal angle between AD and vertical line when a torque M applied.

A simple force balance along the medium plane $O - O'$ gives the following expression:

$$T_1 + T_2 = P[R_1(1 - \cos\theta_1) + W_0\cos\alpha + R_2(1 - \cos\theta_2)] \tag{36}$$

where T_1 and T_2 are the tensions in the fabric membranes.

We now balance the torque induced by the tensile forces T_1 and T_2, and the pressure P with respect to the middle of the symmetric plane of $O - O'$, which leads to:

$$M = (T_2 - T_1)\frac{1}{2}\left[R_1(1 - \cos\theta_1) + W_0\cos\alpha + R_2(1 - \cos\theta_2)\right] L \tag{37}$$

Laplace law imposes:

$$P = \frac{T_1}{R_1} = \frac{T_2}{R_2} \tag{38}$$

Combining Eqs. 37, 38, the applied torque can finally be written as:

$$M = \left(\frac{W'^2}{\theta_2^2} - \frac{W^2}{\theta_1^2} \right) \frac{PL}{8} \tag{39}$$

To derive the torque M, we thus need to obtain the values of the two unknowns θ_1 and θ_2. Note that this last relationship implies $W_0 \cos\alpha = R_1 \cos\theta_1 + R_2 \cos\theta_2$. In other words, the centers of the arc of circles AB and CD coincide.

After inputting the geometrical relationships (Eqs. 32-35) and the force balance (Eq. 36) into Eq. 38, we finally obtain a system of two equations and two unknowns θ_1 and θ_2:

$$\frac{W'}{H}\,\theta_1 \sin\theta_2 - \frac{W}{H}\,\theta_2 \sin\theta_1 - \frac{2\theta_1\theta_2}{\cos\beta} = 0 \quad \frac{W'}{H}\,\theta_1 \cos\theta_2 + \frac{W}{H}\,\theta_2 \cos\theta_1 - \frac{2\theta_1\theta_2}{\cos\beta} = 0 \tag{40}$$

As a starting point to numerically solve the system, we take the case with no applied torque, that is, $\alpha = \alpha_0$. Once $theta_1$ and $theta_2$ are determined, the corresponding value of $alpha$ is deduced from the following combination of Eqs. 32-34:

$$\sin\alpha = \frac{W'}{W_0}\frac{\sin\theta_2}{2\theta_2} - \frac{W}{W_0}\frac{\sin\theta_1}{2\theta_1} \tag{41}$$

and the value of the deflection angle γ from $\gamma = 2(\beta - \alpha)$. Experimental data obtained with a range of geometrical parameters and different applied pressure are in excellent agreement with the theoretical predictions (Figs. S10 and S11).

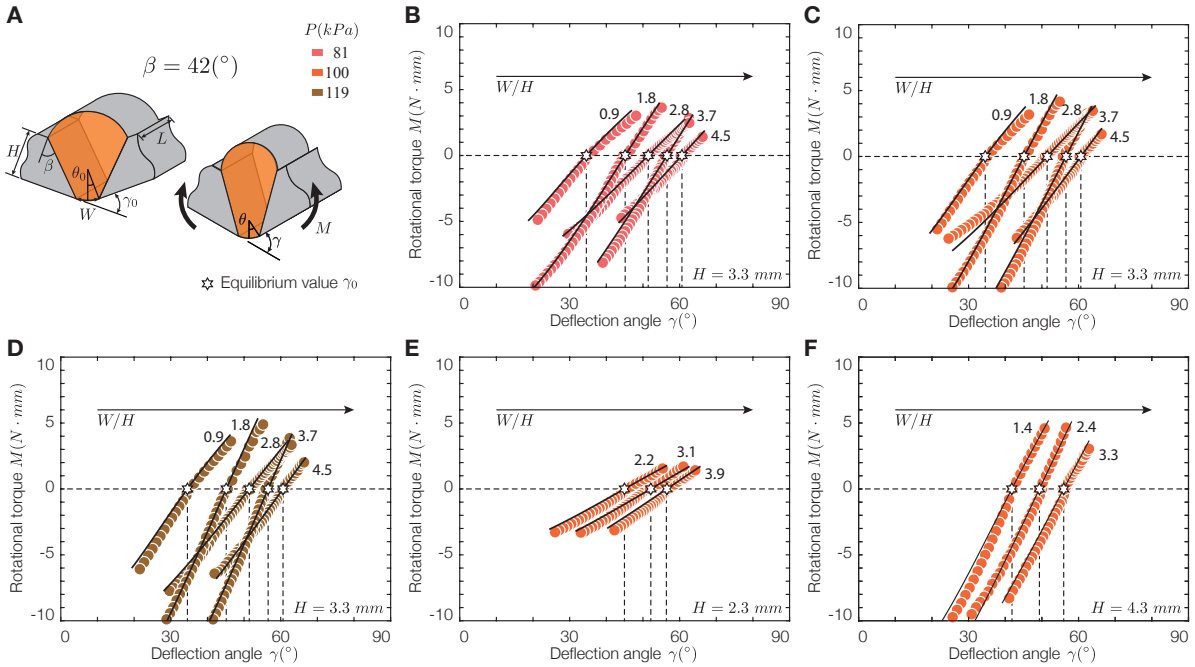

Figure S10: Bending test for symmetric cells ($\beta = 42°$) **(A)** Starting from an equilibrium deflection γ_0, applying a torque M results in a new deflection γ. **(B-F)** Torque vs deflection angle for cells of different heights H and dimensionless widths W/H for different applied pressures P (brown data points, 119 kPa; orange, 100 kPa; pink, 81 kPa). Comparison with theoretical prediction (solid black lines).

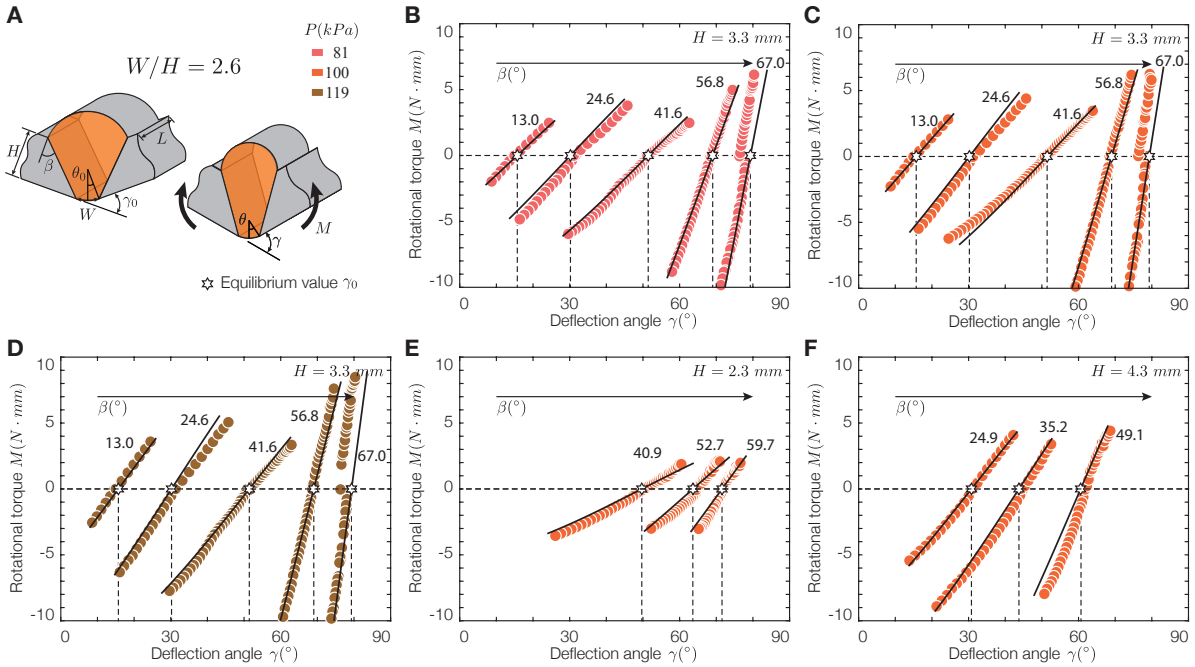

Figure S 11: Bending test for symmetric cells ($W/H = 2.6$) **(A)** Starting from an equilibrium deflection γ_0, applying a torque M results in a new deflection γ . **(B-F)** Torque vs deflection for cells of different heights H and dimensionless widths W/H for different applied pressures P (brown data points, 119 kPa; orange, 100 kPa; pink, 81 kPa). Comparison with theoretical prediction (solid black lines).

4 Assembly of unit cells: shape programming and inverse problem

From an annulus with a radial cut to a truncated cone

We consider an annulus with an outer radius R_0. pneumatic Gaussian cells (of triangular cross-section) each panel folds by an angle γ upon inflation, while azimuthal distances remain unchanged (Fig. S12A). As a result, we obtain a cone of half angle ϕ. In the limit of large values of N, each panel can be considered as an infinitesimal element the bending curvature at the outer edge of the cone thus follows:

$$\kappa = \frac{d\gamma}{ds} \simeq \frac{\gamma}{2\pi R_0/N} \tag{42}$$

Basic geometry relates this bending curvature to the cone angle:

$$\frac{1}{\kappa}\cos\phi = R_0 \sin\phi \tag{43}$$

which leads to

$$\tan\phi \simeq \frac{2\pi}{N\gamma} \tag{44}$$

As the perimeter of the initial flat annulus is preserved, we obtain an overlap angle θ^+ as the structure folds:

$$(2\pi + \theta^+)R_0 \sin\phi = 2\pi R_0$$

leading to

$$\theta^+ = 2\pi\left(\frac{1}{\sin\phi} - 1\right) \tag{45}$$

We now consider a configuration where the initial flat annulus is divided into N radial cells of rectangular cross-section (Fig. S12B). Upon inflation the panels do not fold but the azimutal direction contracts by an effective ratio:

$$\lambda_{eff} = 1 + (\lambda - 1)\frac{NW}{2\pi R_0} \tag{46}$$

where W is the width and λ the contraction of an elementary cell at the outer diameter.

As a consequence, the annulus remains flat and opens by an angle:

$$\theta^- = 2\pi(1-\lambda_{eff}) = (1-\lambda)\frac{NW}{R_0} \tag{47}$$

Morphing a flat annulus into a cone requires both bending and metric change. In other words, the overlap and deficit angles θ^+ and θ^- corresponding to the both deformations have to match as in the example illustrated in Fig. 4C.

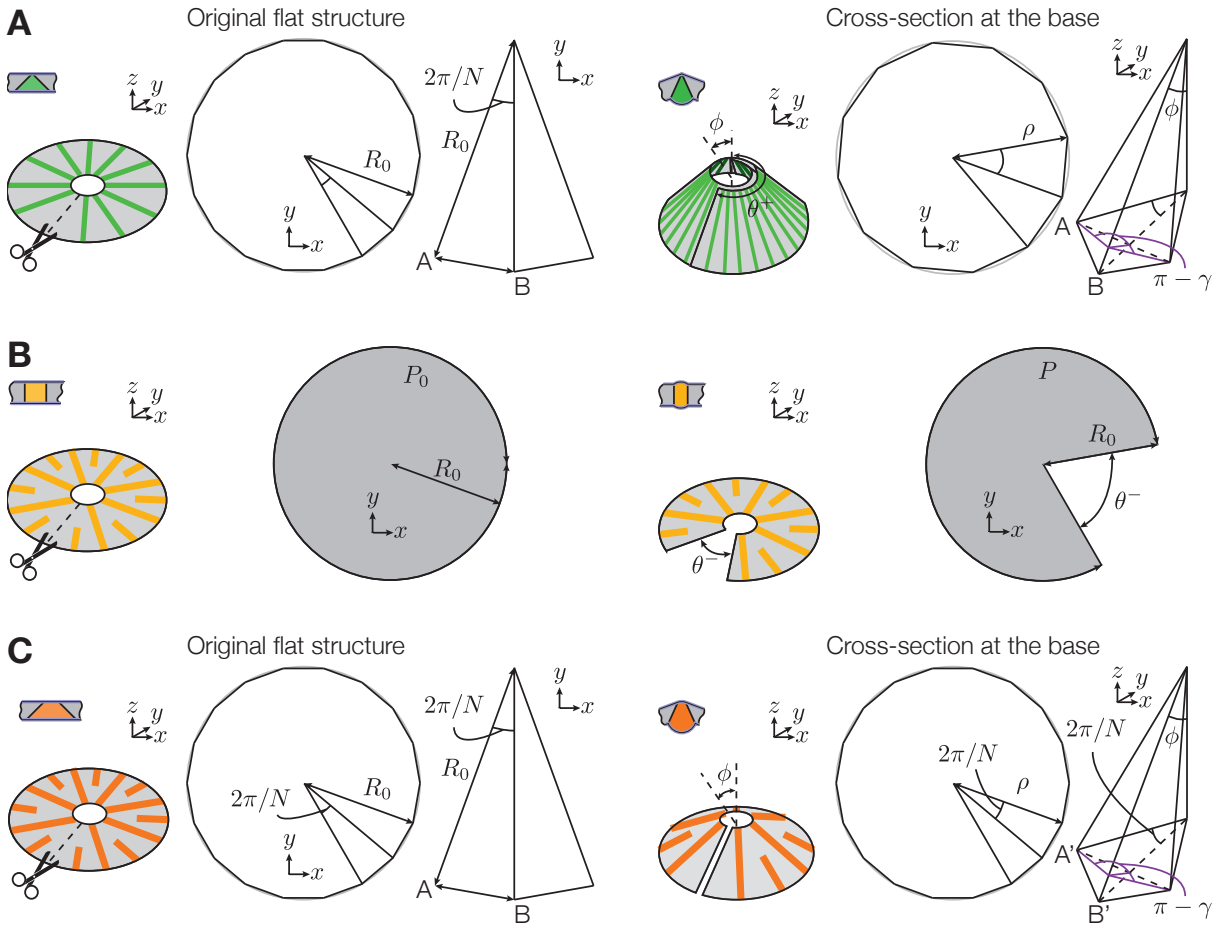

Figure S12: A flat annulus with a cut morph into a flat annulus sector with angular deficit $\theta = 2\pi(1-\lambda)$ and a truncated cone with a half angle $\tan\phi = \lambda$. See Movie S3 of a deploying cone.

Inflatable curve-folded origami structure

We now consider the wrapping of a thin, flat membrane around a central hub, as proposed by by Guest and Pellegrino (1992). The structure is here composed of 6 pairs of triangular panels, following a design reminiscent of an optical diaphragm. Each pair is divided into 11 parallel elements actuated by 10 cells of triangular cross-section. These cells act as "mountain" or "valley" folds in traditional origami (Fig. S13A). "Mountain" and "valley" panels alternate and thus tend to induce opposite bending directions. Upon inflation, the structure wraps around a central hexagon. In the illustrated example, an initial flat disk of radius $R_0 = 65$,mm self-compacts into a cylinder of typical radius $R \simeq 27$ mm (Fig. S13B).

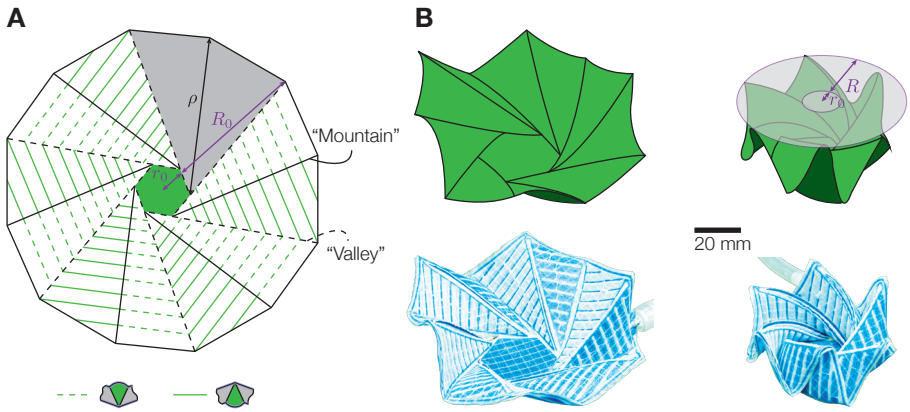

Figure S 13: Inflatable space origami: (A) Design of the fold patterns inspired by Starshade project. **(B)** wrapping of a flat, thin membrane around a central hub upon inflation. See the Movie S1 of the folding of the structure upon inflation.

Programming Miura-ori plate

Fig. S14A describes the basic outlines of a Miura-ori structure in its flat configuration with an elementary element shaded in grey. The structure is composed of alternating parallelogram panels connected by "mountain" or "valley" creases. The actuation of an elementary element is described in Fig. S14B. The parallelograms are characterized by their edges of length a and

b, and the shear angle β. Upon actuation, the crease in the symmetry axis adopts an angle $\psi_1 = \pi = \gamma_1$ while the side creases reach a angle $\psi_2 = \pi - \gamma_2$. Viewed from above, the angle of the V shape of the structure changes from 2β to θ. As such origami structure has only one degree of freedom, the 3 angles are related. The V shape angle θ may be taken as the closing parameter. Following Schenk & Guest (2013), we obtain:

$$\sin(\psi_1/2) = \frac{\sin(\theta/2)}{\sin\beta} \tag{48}$$

$$\sin(\psi_2/2) = \frac{\tan(\theta/2)}{\tan\beta} \tag{49}$$

Similarly, the varying length scales can be parameterized with θ:

$$h = a\frac{\sqrt{\sin^2\beta - \sin^2\frac{\theta}{2}}}{\cos\frac{\theta}{2}} \tag{50}$$

$$w = 2a\frac{\cos\beta}{\cos\frac{\theta}{2}} \tag{51}$$

$$l = 2b\sin\frac{\theta}{2} \tag{52}$$

As a consequence, the longitudinal contraction ration of the whole structure is set by $w/2a = \cos\beta/\cos(\theta/2)$, while the effective contraction in the transverse direction follows $l/2b\sin\beta = \sin(\theta/2)/\sin\beta$.

In the illustrated , we chose $a = 40$mm, $b = 40$mm, $\beta = 36°$. We targeted for the V angle $\theta = 67°$ and the folding angles $\gamma_1 = \pi - \psi_1$ and $\gamma_2 = \pi - \psi_2$ where programmed following Eqs. 48, 49, respectively. See Movie S5 for an actuation demonstration.

General recipe to select isometric shapes

Proof of Gaussian curvature invariant during the transformation between helicoid to catenoid

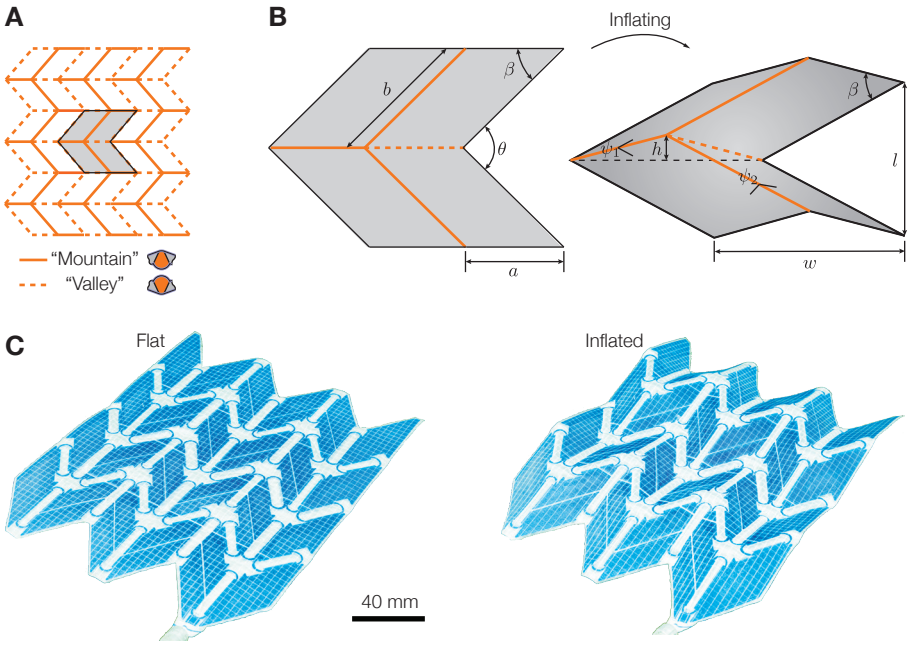

Figure S14: Self-folding Miura-Ori structure: (A), design of the folding pattern with "mountain" and "valley" creases. **(B)** geometry of an elementary unit. **(C)** Pictures of a flat and actuated structure. A dynamical version is available in the Movie S5.

We start by considering the reference configuration of a material surface, namely, a two-dimensional surface immersed in $\mathbb{R}^3$ and its deformations (helicoid or catenoid). The deformed configuration of this material surface will be given by its coordinates $\chi = (x, y, z)$ in the 3D space as a function of two parameters (p, q) defined on a given interval.

We are then interested in deformed configurations, where the helicoid can be continuously deformed into a catenoid by the isometric transformation, given by their parametric equations:

$$x(p,q) = \cos\alpha \sinh q \sin p + \sin\alpha \cosh q \cos p \tag{53}$$

$$y(p,q) = -\cos\alpha \sinh q \cos p + \sin\alpha \cosh q \sin p \tag{54}$$

$$z(p,q) = p\cos\alpha + q\sin\alpha \tag{55}$$

where $\alpha = 0$ corresponds to a helicoid and $\alpha = \pi/2$ to a catenoid.

We now consider two neighbouring points χ and $\chi + \mathrm{d}\chi$ on the surface, the distance ds between

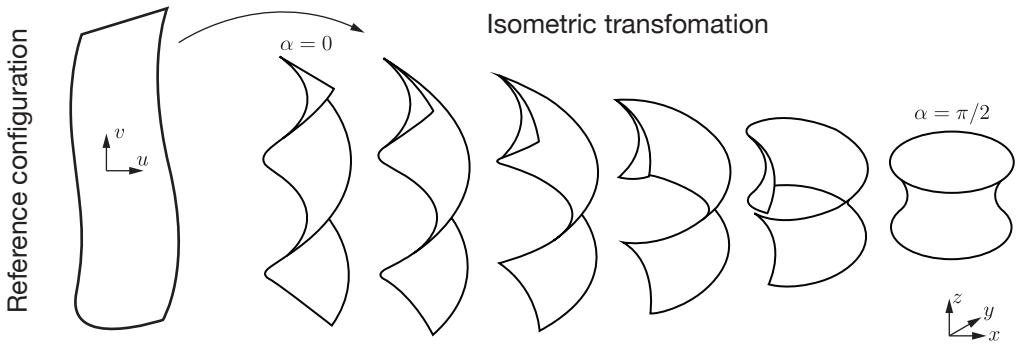

Figure S15: The reference configuration of a material surface and its deformations (isometric transformation between helicoid and catenoid shapes)

them reads classically $\mathrm{d}s^2 = \mathbf{d}\chi \cdot \mathbf{d}\chi$. Expressing $\mathbf{d}\chi$ as a function of p and q leads to $\mathbf{d}\chi = \chi_p \mathbf{dp} + \chi_q \mathbf{dq}$, where the subscripts correspond to derivation with respect to the variable. We thus obtain the first fundamental form of a surface:

$$\mathrm{d}s^2 = \chi_p \cdot \chi_p \, \mathbf{dp}^2 + \chi_p \cdot \chi_q \, \mathbf{dpdq} + \chi_q \cdot \chi_q \, \mathbf{dq}^2 \tag{56}$$

Thus, using Eqs. 53-55, we can compute the surface deformation gradient $\mathbf{F}$ and obtain the metric tensors of the material surface in the deformed configurations as:

$$\mathbf{a} = \begin{bmatrix} E & F \\ F & G \end{bmatrix} = \begin{bmatrix} \chi_p \chi_p & \chi_p \chi_q \\ \chi_p \chi_q & \chi_q \chi_q \end{bmatrix} = \begin{bmatrix} \cosh^2 q & 0 \\ 0 & \cosh^2 q \end{bmatrix} \tag{57}$$

Importantly, the metric tensor $\mathbf{a}$ is a here a function of parameter q, independent of transformation parameter α. In other words, the transformation from an helicoid to a catenoid is an isometry. Moreover, the deformed configuration of this material surface in comparison with a flat surface will be given by such mapping: at each point, we stretch the reference by the same amount $\cosh q$ along $[p, q]$ directions.

In order to derive the second fundamental form which defines the shape tensor, we consider a curve $\mathbf{C}$ passing through a point χ on the surface. At this point, the unit tangent $\mathbf{t}$ to the curve

$\mathbf{C}$ belongs to the tangent plane and its curvature $\mathbf{dt}/\mathrm{d}s$ may be projected onto the normal $\mathbf{N}$ of the surface. We call this quantity the normal curvature k_n:

$$k_n = \mathbf{N} \cdot \frac{\mathbf{dt}}{\mathrm{d}s} = \frac{\mathbf{d}\chi \cdot \mathbf{N}}{\mathrm{d}s^2} \tag{58}$$

where the unit normal vector $\mathbf{N}$ reads:

$$\mathbf{N} = \frac{\chi_p \times \chi_q}{|\chi_p \times \chi_q|} = \begin{bmatrix} \cos p/\cosh q, \\ \sin p/\cosh q, \\ -\sinh q/\cosh q \end{bmatrix} \tag{59}$$

By differentiation, we trivially obtain:

$$\mathbf{d}\chi = \chi_p \,\mathrm{d}p + \chi_q \,\mathrm{d}q \tag{60}$$

$$\mathbf{N} = \mathbf{N}_p \,\mathrm{d}p + \mathbf{N}_q \,\mathrm{d}q \tag{61}$$

Inputting these Eq. 57 and Eqs.60,61 in Eq. 58, we get:

$$k_n = \frac{\chi_p \cdot \mathbf{N}_p \,\mathrm{d}p^2 + (\chi_p \cdot \mathbf{N}_q + \chi_p \cdot \mathbf{N}_q)\,\mathrm{d}p\,\mathrm{d}q + \chi_q \cdot \mathbf{N}_q \,\mathrm{d}q^2}{E\,\mathrm{d}p^2 + 2F\,\mathrm{d}p\,\mathrm{d}q + G\,\mathrm{d}q^2} \tag{62}$$

The second fundamental form is simply the numerator of this expression:

$$II = e\,\mathrm{d}p^2 + 2f\,\mathrm{d}p\,\mathrm{d}q + g\,\mathrm{d}q^2 \tag{63}$$

where e, f, g are coefficients of the second fundamental form. Combining Eqs. 53-55 and Eq. 59, the coefficients of the second fundamental form can be derived as:

$$e = \chi_{pp}\mathbf{N} = -\sin\alpha \tag{64}$$

$$f = \chi_{pq}\mathbf{N} = \cos\alpha \tag{65}$$

$$g = \chi_{qq}\mathbf{N} = \sin\alpha \tag{66}$$

Writing them in a matrix form, we get the shape tensor:

$$\mathbf{b} = \begin{bmatrix} e & f \\ f & g \end{bmatrix} = \begin{bmatrix} -\sin\alpha & \cos\alpha \\ \cos\alpha & \sin\alpha \end{bmatrix} \tag{67}$$

The possibility of changing curvature (morphing) of a surface by acting on its metric relies on a remarkable theorem by Gauss, his celebrated theorema egregium, stating that the Gaussian curvature K of a surface (the product of its principal curvatures) can be computed in terms of the coefficients of both fundamental forms:

$$K = \frac{eg - f^2}{EG - F^2} = -\frac{1}{\cosh^4 q} \tag{68}$$

Notably, the Gaussian curvature K here is a function of the parameter q and independent from the transformation parameter α. Thus we can say that Gaussian curvature K at a given point of the surface is invariant during the transformation between helicoid to catenoid, as expected for isometries.

Programming zigzag path for metric change

As reference configuration S_0, we consider a flat material sheet of length L_0 and height H_0. We then focus on its deformed configuration (the axisymmetric surface, i.e. catenoid).This means that we consider a map $(u, v) \mapsto \chi(u, v) \in \mathbb{R}^3$, where $(u, v) \in (L_0, H_0) \subset \mathbb{R}^2$.

The deformed configuration with catenoid shape can be written by assigning a generating catenary curve $[r(v), z(v)]$ in the symmetry plane and an azimuthal displacement $\psi(v)$, leading to:

$$\boldsymbol{\chi}(u, v) = \left\{ r(v) \cos\left(\tfrac{u}{R_0} + \psi(v)\right), r(v) \sin\left(\tfrac{u}{R_0} + \psi(v)\right), z(v) \right\}, \tag{69}$$

$$u \in (-L_0/2, L_0/2), \quad v \in (-H_0/2, H_0/2) \tag{70}$$

where $L_0 = 2\pi R_0$.

The catenary curve $[r(v), z(v)]$ here can be described as:

$$r(v) = a \cosh \frac{z(v)}{a} \tag{71}$$

where $a = r(0)$.

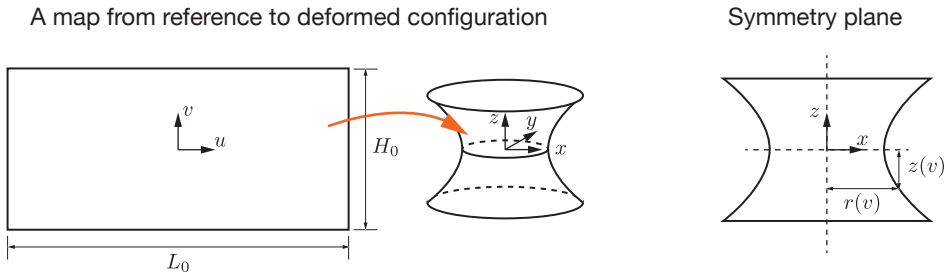

Figure S16: Flat material sheet deformed into a catenoid and cross-sectional view.

By computing its deformation gradient, we can obtain its metric tensor as:

$$g = \begin{bmatrix} E & F \\ F & G \end{bmatrix} = \begin{bmatrix} (r/R_0)^2 & r^2\psi'/R_0 \\ r^2\psi'/R_0 & r'^2 + z'^2 + r^2\psi'^2 \end{bmatrix} \tag{72}$$

where a prime $(\cdot)'$ denotes differentiation with respect to v. Clearly, since the left-hand side in the last equation depends only on v, only metric tensors $g = g(v)$ that are independent of u (axisymmetric actuation) are compatible with Eq. 69.

To achieve such deformation, let us consider a contraction with principal directions along the coordinate lines using zigzag pattern:

$$g = \begin{bmatrix} \Lambda_1^2 & 0 \\ 0 & \Lambda_2^2 \end{bmatrix} \tag{73}$$

where $\Lambda_1 = \Lambda_1(u, v) \in (0, +\infty)$ and $\Lambda_2 = \Lambda_2(u, v) \in (0, +\infty)$ are the stretches along the $u-$ and $v-$coordinate lines, respectively. The contraction of the pneumatic membrane is a special case of fixed area ratio by setting $\Lambda_1\Lambda_2 = \lambda_\sigma$.

Following theorema egregium, the Gaussian curvature K here can be computed in this particular case as:

$$K_c = -\frac{1}{\lambda}(\Lambda_1^2)'' \tag{74}$$

Investigating the unit cell of our periodic zigzag, we have:

$$\Lambda_1 = \lambda_\parallel^2 \cos^2\theta_0 + \lambda_\perp^2 \sin^2\theta_0, \quad \Lambda_2 = \frac{\lambda_\Sigma}{\Lambda_1} \tag{75}$$

where $\lambda_\parallel = 1$ is active stretch along the director field, and$\lambda_\perp < 1$ in the perpendicular direction. θ_0 is the initial zigzag angle.

Submitting Eq. 73 into Eq. 72, we obtain:

$$r(v) = \Lambda_1(v) R_0\,, \tag{76}$$

$$\psi'(v) = 0\,, \tag{77}$$

and

$$z'(v) = \pm\frac{1}{\Lambda_1(v)}\sqrt{\lambda^2 - (R_0\Lambda_1(v)\Lambda_1'(v))^2}\,, \tag{78}$$

Solving Eqs. 71, 74, and 76-78, we obtain:

$$\Lambda_1 = \Lambda_1(v) \tag{79}$$

$$K = K(v) \tag{80}$$

Starting from a given distribution $\Lambda_1(v)$, the zigzag channels are designed in practice in the following way: Submitting Eq. 79 to Eq. 75 we deduce that

$$\sin(\theta_0) = \sqrt{\frac{\lambda_\parallel^2 - \Lambda_1^2}{\lambda_\parallel^2 - \lambda_\perp^2}} = \sqrt{\frac{1-\Lambda_1^2}{1-\lambda_\perp^2}} \tag{81}$$

and zigzag angle $\theta_0(v)$ as a function of v.

The actual zigzag path is obtained as:

$$Z(v) = U(v)T(v) \tag{82}$$

where $T(v)$ is a symmetric triangle wave with period $P = H_0/N =$ with extremal values ± 1. In practice, tilted Thermoplastic Polyurethane (TPU) walls are 3D-printed on the first layer of TPU coated fabric following such zigzag path.

The amplitude $U(v)$ follows:

$$U = \frac{P}{4\tan(\theta_0)}$$

and is drawn in blue color in Fig. S17C.

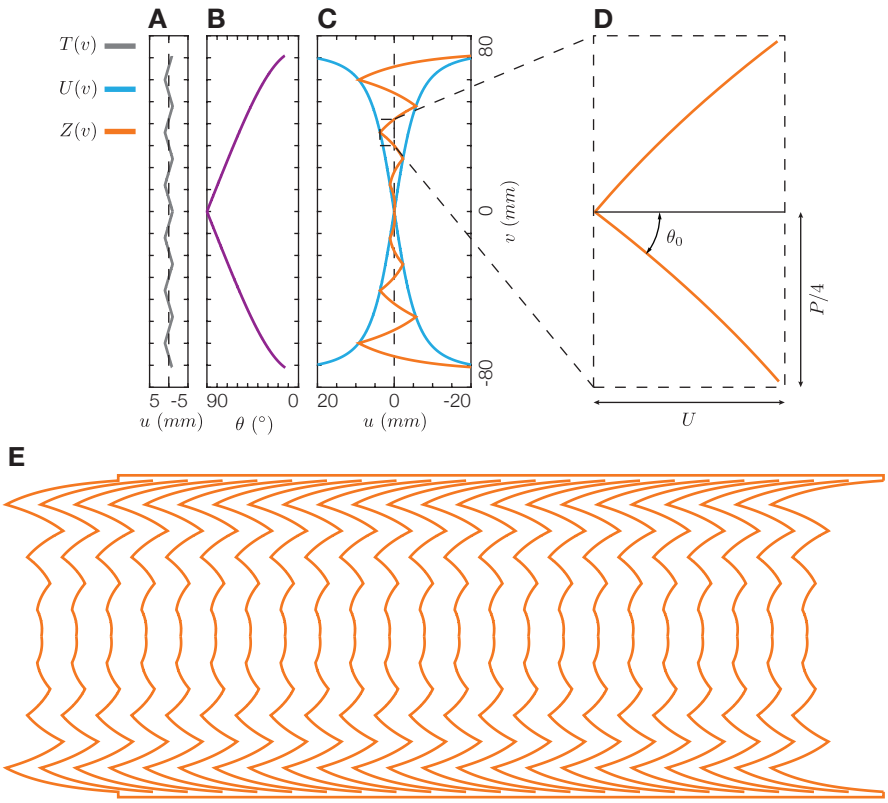

Figure S17: Generation of the zigzag pattern: (A) A symmetric triangle wave with period P and with extremal values 1. **(B)** Actual zigzag angle θ_0 as a fuction of v. **(C)** Amplitude U of actual zigzag path (blue) and actual zigzag path (red). **(D)** Half period of actual zigzag path. **(E)** Complete zigzag pattern programmed to morph into helicoid or catenoid. Scale bar: 100 mm.

Since the isometric helicoid has the same metric as the described catenoid, the same zigzag pattern can be used for both of them.

Programming curvature following vectors normal to zigzag path

In the reference configuration, we consider a pair of neighbouring points χ and $\chi + \mathbf{d}\chi$ on the

finite surface element, where $\mathbf{d}\chi$ is normal to the tangent vector of zigzag path, ϕ is the angle between $\mathbf{d}\chi$ and $\mathbf{du}$ ($\mathbf{du}$, $\mathbf{dv}$ are orthogonal unit vectors in the direction u and v, respectively). Following basic geometry, we obtain:

$$\tan\phi = \frac{\chi_v}{\chi_u} \tag{83}$$

Inflation induces a contraction in both directions u and v, with respective contraction ratios Λ_1 and Λ_2. As a consequence, the angle ψ between the direction of the pair of selected points and $\mathbf{du}$ reads:

$$\tan\psi = \frac{\Lambda_2\chi_v}{\Lambda_1\chi_u} \tag{84}$$

As catenoid is a minimal surface, its mean curvature H and Gaussian curvature K read:

$$H = \frac{k_1 + k_2}{2} = 0 \tag{85}$$

$$K = k_1 k_2 \tag{86}$$

where k_1,and k_2 are the principal curvatures.

Inputting Eqs. 85 and 86 into Eq. 80, we deduce the principal curvatures as a function of v:

$$k_1(v) = -k_2(v) = \sqrt{K(v)} \tag{87}$$

In the case of the catenoid, principal curvatures k_1 and k_2 are in the direction u and v, respectively (Fig. S18). One important fact about the principal directions and principal curvatures is that they respectively correspond to eigenvectors and eigenvalues of the shape operator. The principal curvatures are sufficient to describe locally the shape as any tangent vector can be expressed as a linear combination of the principal directions. In particular, if k_n is a unit vector offset from by an angle θ, the associated normal curvature is given by:

$$k_n = k_1\cos^2(\theta) + k_2\sin^2(\theta) \tag{88}$$

As one can verify using the relationships above.

Combining Eqs. 79, 80, 82, 83, 87 and 88, we can compute normal curvature $K_{c\perp}$ following $\mathbf{d}\chi$ normal to the tangent vector of the zigzag path:

$$k_{c\perp}(v) = \sqrt{K(v)}\frac{\Lambda_1^2(v) - \lambda^2 U'^2(v)}{\Lambda_1^2(v) + \lambda^2 U'^2(v)} \tag{89}$$

where a prime $(\cdot)'$ denotes differentiation with respect to v.

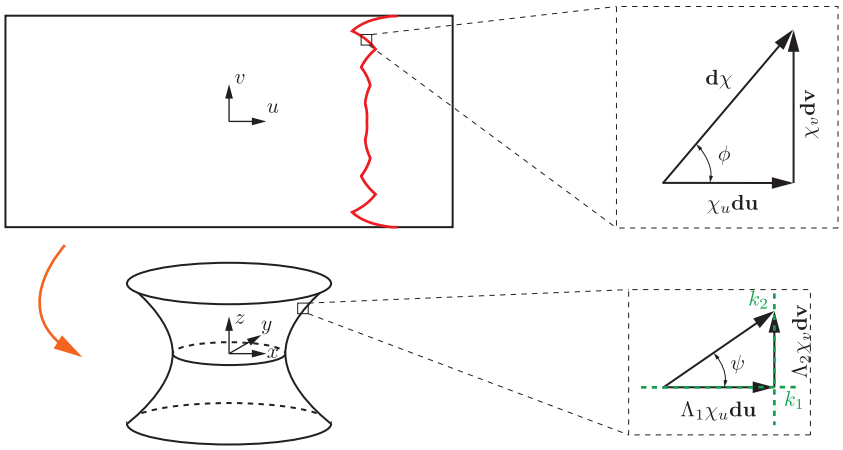

Figure S18: Computing locally the curvature $k_{c\perp}$ normal to the zigzag path (red color, the same one as shown in Fig. S17) in a catenoid shape.

In the case of the helicoid shape, the principal curvatures k_1 and k_2 are in the directions offset from u and v by an angle of $45°$, respectively (Fig. S19). As the helicoid have the same Gaussian curvature K and mean curvature H as a catenoid, combining Eqs. 79, 80, 82, 83, 87 and 88, we can compute normal curvature $K_{h\perp}$ following $\mathbf{d}\chi$ normal to the tangent vector of zigzag path.

$$k_{h\perp}(v) = k_1(v)\cos^2\left(\psi - \frac{\pi}{4}\right) + k_2(v)\sin^2\left(\psi - \frac{\pi}{4}\right) = -\frac{2\lambda\sqrt{K(v)}U'(v)\Lambda_1^2(v)}{\Lambda_1^4(v) + \lambda^2 U'^2(v)} \tag{90}$$

This curvature is then used as a target for the corresponding cell, setting its internal design.

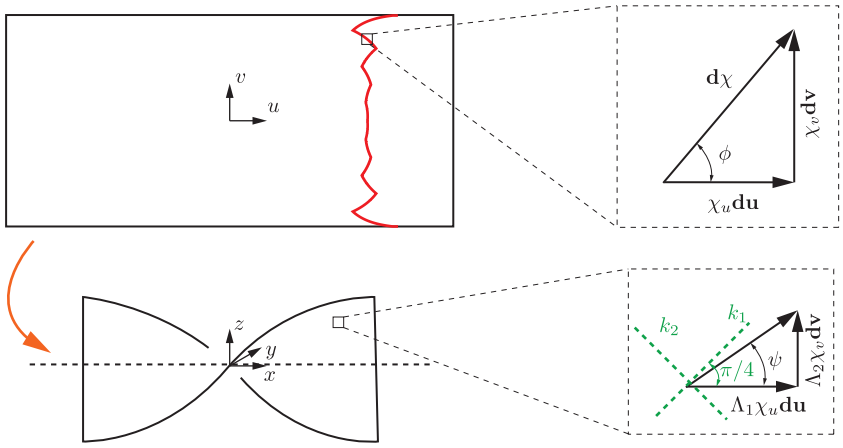

Figure S19: Computing locally the curvature $k_{h\perp}$ normal to the zigzag path (red color, the same one as shown in Fig. S17) in a helicoid shape.

5 Scalability and performances

In this section we provide some design rules and discuss scalablility and performances of our system using scaling law arguments.

Maximum internal pressure

Increasing the internal pressure P provides a larger stiffness to the pressurized structure. We discuss here the maximum admissible value. A first point is that our analysis is restricted to cases where the fabric can be considered as inextensible. The strains in the fabric are on the order of PH/Y, where Y is the membrane stiffness of the fabric (product of Young modulus with thickness). Our description is only valid if $P \ll Y/H$. A second limit for pressure, more relevant in our study, is the condition for detachment of the fabric from the TPU-printed structure. We note that the tension in the fabric is on the order of PW. Assuming that detachment occurs for a critical value of this tension (which strongly depends on material and manufacturing techniques), we find that the maximal pressure is inversely proportional to the size of the cells, a feature that constrains the attainable stiffness of cells.

Stiffness : Imposed pressure versus constant fluid mass

In this study we focus on a system subject to a constant internal pressure P. It is also possible to inflate the system up to the same desired pressure, and seal it, so that the mass of the internal fluid is constant (but not its pressure). We argue here that the linear response of the system (stiffness of the equilibrium) is the same in both cases, independently of the fluid compressibility.

We consider an approach based on energy balance, for a system such as in Figure S7 ($\beta = 0$).

In the case of an imposed pressure P, the energy of the system is

$$U(S) = -PV(S),$$

where the volume $V(S)$ is a function of the inter-wall distance S (in the limit of inextensible fabric). The equilibrium obeys $dU/dS = -PdV/dS = 0$, which maximizes the volume of the cell. The stiffness k of the system can simply be computed as:

$$k = \frac{d^2U}{dS^2} = -P\frac{d^2V}{dS^2}$$

We now turn to the case where the fluid is injected up to the same pressure P and then the inlet is sealed, maintaining the mass of fluid constant inside the structure. The energy U_f of this mass of fluid at a constant temperature is a function of its available volume $V(S)$. At equilibrium,

$$\frac{dU_f(V(S))}{dS} = \frac{\partial U_f}{\partial V}\frac{dV}{dS} = 0$$

where we note that by definition $\frac{\partial U_f}{\partial V} = -P$. Again we find that equilibrium occurs when the volume is maximized. The stiffness here obeys:

$$\frac{d^2U_f}{dS^2} = \frac{\partial^2 U_f}{\partial V^2}\left(\frac{dV}{dS}\right)^2 + \frac{\partial U_f}{\partial V}\frac{d^2V}{dS^2}$$

We note that the first term vanishes at equilibrium, so that the stiffness is again $k = -P\frac{d^2V}{dS^2}$, depending only on the equilibrium pressure and on the geometrical function $V(S)$.

We deduce that within the assumption of inextensibility, the stiffness of the system, that is the linearized mechanical response of the system close to equilibrium, does not depend on the condition of inflation (imposed pressure, constant mass), but only on the intitial internal pressure and on the geometry of the cell.

Structural stiffness vs smoothness

A given target surface shape, can be approximated by different distributions of Gaussian cells.

A natural question is how to select the separation between cells, which plays the role of a discretization distance. Geometrical accuracy favours the finest possible steps and therefore the largest number of cells. However, we show here that there is a trade-off when it comes to structural stiffness, which is larger when using fewer larger Gaussian cells.

We consider the simple shape of a cylinder with radius of curvature R_0 (curvature $\kappa_0 = R_0^{-1}$), and define ℓ the discretization distance (spatial distance between the center of the cells) assumed as uniform. We also consider for simplicity triangular cells $W = 0$ which are sufficient to provide a deflection compatible with a developable target shape. For a good geometrical approximation of the cylinder, each cell has to provide a folding angle $\gamma = \ell/R_0$, which thus determines the internal geometry of the cell, i.e the internal angle $\beta(\ell)$, from equation (1) in the main text).

The effective bending stiffness $B_{eq}(\ell)$ of this equivalent plate can be inferred from the following. When a pure torque M is applied, it will modify the folding angle of each cell by $\Delta\gamma = M/K_r$, where K_r is the angular stiffness of the cells (set by equation (4) in main text). The curvature becomes $\kappa = (\gamma + \Delta\gamma)/\ell$, so that the change in curvature is $\Delta\kappa = M/(K_r\ell)$. Finally, we find that this hybrid plate has an equivalent bending stiffness

$$B_{eq}(\ell) = \ell K_r(\ell)$$

Note that $K_r(\ell)$ depends in a non-trivial way on the step length ℓ because the internal geometry of the cell $\beta(\ell)$ must be adjusted differently depending on the discretization length. As a matter of fact, the stiffness of cells increases for smaller deflection angle $\gamma \ll 1$, (see lower left corner in figure 3G of the main text), and therefore $K_r(\ell)$ increases for small ℓ. In Fig. S20, the nondimensional equivalent bending stiffness $B_{eq}(\ell)/PLH^3$ is plotted as a function of the discretization length ℓ for different choices of the target radius of curvature R_0. It is seen that the smoother the plate (i.e. the smaller ℓ), the lower is its equivalent stiffness.

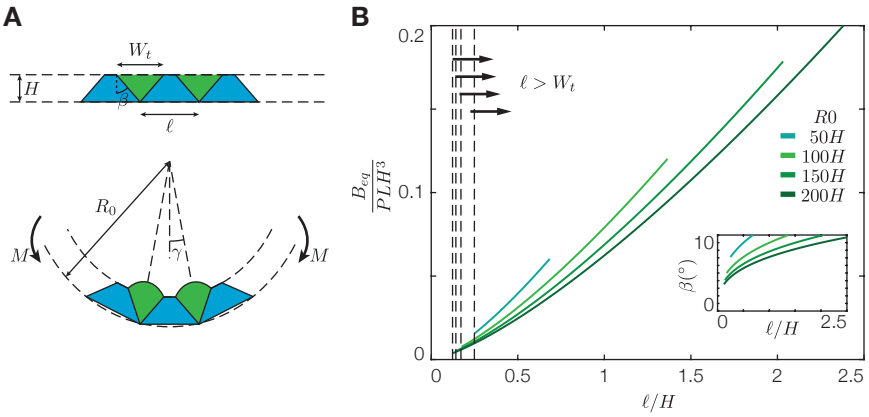

Figure S 20: Effective bending stiffness of a plate programmed to take the shape of a cylinder with radius R_0 as a function of discretization parameter ℓ/H. Smoother shapes involve more hinges and are therefore softer (for a fixed pressure) than coarser shapes with larger spacing ℓ between centers of the cells.

This trend is also true when it comes to stretching stiffness, which is most simply estimated for an assembly of rectangular cells ($\beta = 0$) separated by rigid segments. The effective Young modulus of such a plate is simply given by:

$$E_{eq} = E_c \frac{\ell}{W}$$

(assuming that the building material has a much larger Young modulus than the internal pressure). Again, the effective stiffness vanishes when the discretization is made more accurate (as ℓ goes to zero).

As a conclusion, we find that smoothness is obtained at the cost of a lower stiffness (for a fixed pressure). There is no optimal cell number, and depending on the application, one should decide for a smoother or a stiffer plate. This conclusion is somewhat mitigated by the fact that, for a given distribution of cells, a larger internal pressure provides a larger stiffness of the structure.

Deployment time

The deployment dynamics of such a structure depends primarily on the inflation rate of the

pressure source (how fast can the fluid be filled into the structure) and on the geometry of the network of connected airways (which dictates the pressure losses). In addition, the time required to reach the deployed equilibrium is also bounded by the inertia of the structure. A typical vibration period for an elastic structure with length span $\mathcal{L}$, width L, thickness H, material density ρ and bending stiffness B is $\tau \sim \mathcal{L}^2\sqrt{\rho LH/B}$. In our case, the bending stiffness B depends both o on pressure and geometrical parameter, but a simplified estimate provides $B \sim PLH^3$. Finally, the deployment time scales as

$$\tau \sim \sqrt{\frac{\rho}{P}}\frac{\mathcal{L}^2}{H}$$

We see that structures with large span $\mathcal{L}$, bearing more inertia, take more time to reach their deployed equilibrium. This effect can be in principle counterbalanced by using larger pressure P which tends to shorten the deployment time. In practice, the $P^{-1/2}$ and $\mathcal{L}^2$ dependence shows that a very large increase of pressure is needed to balance a change in size.

6 Captions for Videos

Movie S1:

Fabrication and pneumatic deployment of a structure based on Gaussian cells.

Thermo-Plastic Urethane (TPU) building blocks are 3D printed on a first layer of TPU-coated fabric (extrusion temperature $210°$C, displacement of printing head at 12 mm/s). A vacuum pump is used to maintain the fabric sheet flat on the printing board, and to avoid sliding (fabrication process played fast forward at 8x speed). An additional layer of the same fabric is heat-sealed on the top of the printed structure with a heating press (at a temperature of $184°$C for 10s). Finally, Pneumatic Gaussian cells embedded in the thin sandwich are connected to a pressure source. Upon pressure, the initially flat structure morphs into a complex shape such as a "starshade" model (actuation played at 2x speed).

Movie S2:

Programming developable surfaces.

Developable shapes based on triangular cells: (i) "S" shape with opposite constant curvatures; (ii) Spiral with linearly increasing curvature; (iii) Curling shape with variable curvature direction; (iv) Developable helicoid obtained when generating lines are tangent to the initial central circle (movie played at 2x speed).

Movie S3:

Morphing a disk into a cone.

A sectioned annulus with a radial cells morph into (i) a truncated cone with angular surplus when pure bending is programmed with triangular cells ; (ii) a flat annulus sector with angular deficit when pure metric change is programmed with rectangular cells; (iii) a perfect truncated

cone when bending and metric changes are programmed simultaneously (movie played at 2x speed).

Movie S4:

Selection between isometric shapes (helicoid and catenoid).

The same metric change provided by a programmed zigzag pattern leads to degenerated isometric shapes from helicoid to catenoid. Controlling the local bending breaks the degeneracy (helicoid actuation played at 1.5x speed, catenoid actuation played at 2x speed).

Movie S5:

Self-actuated Miura-ori panel.

Gaussian cells here function as stiff "mountain" or "valley" creases. The resulting structure is stiff enough to sustain a total load of 1 kg (movie played at 2x speed).

Movie S6:

Towards shape morphing robotics: Manipulating solids

Upon inflation, a flat stripe bends into a curved gutter track, allowing for the manipulation and transport of objects such as a rubber ball of diameter 40 mm and weight 25 g.

Volcano shaped actuator: the initially flat disk is actuated in a fraction of second as a cylinder rolls over it at 10 cm/s. The cylinder (weight 40 g) remains trapped inside the deployed crater (movie played at 1.5x speed).

Movie S7:

Towards shape morphing robotics: Manipulating liquids

Upon inflation, a flat stripe bends into a curved gutter track allowing to transfer liquid from a

container to a different one. Liquids spill out when releasing internal pressure, which demonstrates the significance of surface morphing robotics. In this case, both principal curvatures are programmed to bend in the same direction, leading to positive Gaussian curvature (movie played at 1.5x speed).